CA1-projecting subiculum neurons facilitate object-place learning

Yanjun Sun⁰, 1,11,12</sup>, Suoqin Jin⁰, 2,12</sup>, Xiaoxiao Lin¹, Lujia Chen¹, Xin Qiao¹, Li Jiang¹, Pengcheng Zhou⁰, Kevin G. Johnston², Peyman Golshani^{4,5}, Qing Nie², Todd C. Holmes³, Douglas A. Nitz⁰, and Xiangmin Xu⁰,6,9,10*

Recent anatomical evidence suggests a functionally significant back-projection pathway from the subiculum to the CA1. Here we show that the afferent circuitry of CA1-projecting subicular neurons is biased by inputs from CA1 inhibitory neurons and the visual cortex, but lacks input from the entorhinal cortex. Efferents of the CA1-projecting subiculum neurons also target the perirhinal cortex, an area strongly implicated in object-place learning. We identify a critical role for CA1-projecting subicular neurons in object-location learning and memory, and show that this projection modulates place-specific activity of CA1 neurons and their responses to displaced objects. Together, these experiments reveal a novel pathway by which cortical inputs, particularly those from the visual cortex, reach the hippocampal output region CA1. Our findings also implicate this circuitry in the formation of complex spatial representations and learning of object-place associations.

he role of the hippocampus in spatial cognition and episodic memory has frequently been examined by reference to three prominent schemes by which it is anatomically organized: the trisynaptic pathway, the transverse axis and the longitudinal axis¹⁻³. Historically, the greatest focus has been to examine its function along the trisynaptic pathway and to consider it as a feed-forward, unidirectional circuit. However, new viral-genetic-based mapping approaches for examining connectivity between structures are poised to identify novel circuits within and between the hippocampus and the cortex^{4,5}. In principle, such circuits may serve to broaden the scope of neural functions carried out by interactions between the hippocampus and the cortex, complementing neural processing along the trisynaptic pathway and across the transverse and longitudinal axes.

In examining how hippocampal output may affect cortical targets, emphasis is often placed on the subregion CA1 as the primary output. However, the subiculum (SUB) subregion of the hippocampal formation can be considered as a continuation of the trisynaptic or 'canonical' pathway through the hippocampus. The SUB receives dense input from the CA1 and the entorhinal cortex (EC), and sends efferents to areas such as the retrosplenial cortex and the perirhinal cortex. These cortical targets are critically implicated in multiple forms of spatial cognition and memory ^{6–8}. The SUB therefore stands as a second major output subregion of the hippocampus whose function remains elusive despite early work implicating the SUB in spatial processing that is necessary for navigational performance.

Recent studies have identified a prominent return or 'non-canonical' projection from the SUB to the CA1 (refs. ^{4,5}). The projection is organized according to the transverse axis that splits the

subregion CA1 into distal and proximal components⁵. The functional role of this pathway has been considered only with respect to theta-frequency oscillations that temporally organize nearly all hippocampal spiking dynamics¹⁰. These data challenge traditional views that emphasize a unidirectional projection between the CA1 and the SUB, and identify a feedback circuit by which the SUB may directly modulate CA1 dynamics.

In the present work, we examine the synaptic circuit organization and function of the SUB-CA1 back-projection pathway in the mouse. We apply modern anterograde and retrograde tracing techniques to show that visual cortex efferents can directly reach and affect both the hippocampal subregion CA1 and the perirhinal cortex through a subpopulation of SUB neurons. We use genetically targeted neuronal inactivation in conjunction with in vivo GCaMP6-based calcium imaging of the CA1 in freely moving animals to show that CA1-projecting subicular neurons affect the magnitude of CA1 place cell activity. Furthermore, we examine the impact of this circuit on object-location learning within the environment. Activation and inactivation of this specific circuitry yields improvements and impairments, respectively, in the encoding of object-location relationships, a key form of spatial cognition that is relevant to both human and animal navigation.

Results

We first reveal that the cortico-hippocampal circuitry is associated with SUB projections to the CA1. Monosynaptic rabies tracing identified a significant SUB-CA1 back-projection pathway in mice (Fig. 1a-d), as suggested previously in other mammalian species using less strict mapping methods^{11,12}. We operationally defined an

Department of Anatomy and Neurobiology, School of Medicine, University of California, Irvine, Irvine, CA, USA. ²Department of Mathematics and Department of Developmental & Cell Biology, University of California, Irvine, Irvine, CA, USA. ³Department of Statistics and Center for Theoretical Neuroscience, Columbia University, New York, NY, USA. ⁴Department of Neurology, David Geffen School of Medicine, University of California, Los Angeles, CA, USA. ⁵West Los Angeles VA Medical Center, Los Angeles, CA, USA. ⁶Department of Biomedical Engineering, University of California, Irvine, Irvine, CA, USA. ⁷Department of Physiology and Biophysics, School of Medicine, University of California, Irvine, Irvine, CA, USA. ⁸Department of Cognitive Science, University of California, San Diego, La Jolla, CA, USA. ⁹Department of Microbiology and Molecular Genetics, University of California, Irvine, Irvine, CA, USA. ¹⁰Department of Computer Science, University of California, Irvine, Irvine, CA, USA. ¹¹Present address: Department of Neurobiology, Stanford University School of Medicine, Stanford, CA, USA. ¹²These authors contributed equally: Yanjun Sun, Suoqin Jin. *e-mail: nitz@cogsci.ucsd.edu; xiangmin.xu@uci.edu

ARTICLES

input connection strength index (CSI) as the ratio of the number of presynaptic neurons in a brain region of interest (for example, the SUB) versus the number of postsynaptic (starter) neurons in the CA1. Our quantitative analyses showed that SUB inputs to the CA1 are relatively strong, with high circuit connection strengths. The CSI of subicular back-projections to distal CA1 excitatory neurons was quantitatively similar to that of medial EC inputs to proximal CA1 excitatory neurons (CSI values of 1.33 ± 0.27 for SUB to CA1, and 1.51 ± 0.24 for EC to CA1; N = 6 - 7 cases). There was a weak-to-strong SUB input strength gradient along the proximal—distal axis of the CA1, with an input bias to the distal CA1 (ref. 5).

We also used anterograde-directed herpes simplex virus (HSV; H129 strain) transport to identify SUB-CA1 back projections and to determine whether such neurons also send collateral projections to other brain regions (Fig. 1e-l). Selective labeling of CA1-projecting excitatory SUB neurons was achieved by canine adenovirus 2 (CAV2)-mediated retrograde Cre expression¹³. CAV2expressing Cre (CAV2-Cre) was injected into the CA1 to yield the retrograde expression of Cre recombinase in CA1-projecting SUB neurons (Fig. 1e; Supplementary Fig. 1a,b). The Cre-labeled CA1projecting SUB neurons expressed tdTomato using the Ai9 reporter mouse (Supplementary Fig. 1c-e). Excitatory SUB neurons were predominantly labeled, as none of the CAV2-labeled cells in the SUB were GABA-positive, and 90% of CAV2-labeled SUB neurons were immuno-positive for Ca2+/calmodulin-dependent protein kinase II (CaMKIIα) (Supplementary Fig. 1f). The output projections of CA1-projecting SUB neurons were mapped using Credependent anterograde-directed H129 virus. Initial replication of this recombinant H129 strain¹⁴ is dependent on Cre recombination of the expression cassette containing the codon of a modified HSV thymidine kinase gene (TK) and the tdTomato reporter. After Cre recombination, the HSV viral genome permanently expresses TK, and synaptically connected cells are labeled. We used the conservative time control of 48 h post-injection to limit labeling to directly connected postsynaptic neurons¹⁴. CA1 projections from CAV2Cre-labeled SUB neurons were confirmed by the robust postsynaptic labeling of hippocampal CA1 neurons 48 h after H129 viral injection (Fig. 1f-h). Efferents of the CA1-projecting SUB neurons also targeted the perirhinal cortex (Fig. 1i-l), an area strongly implicated in object–place learning¹⁵.

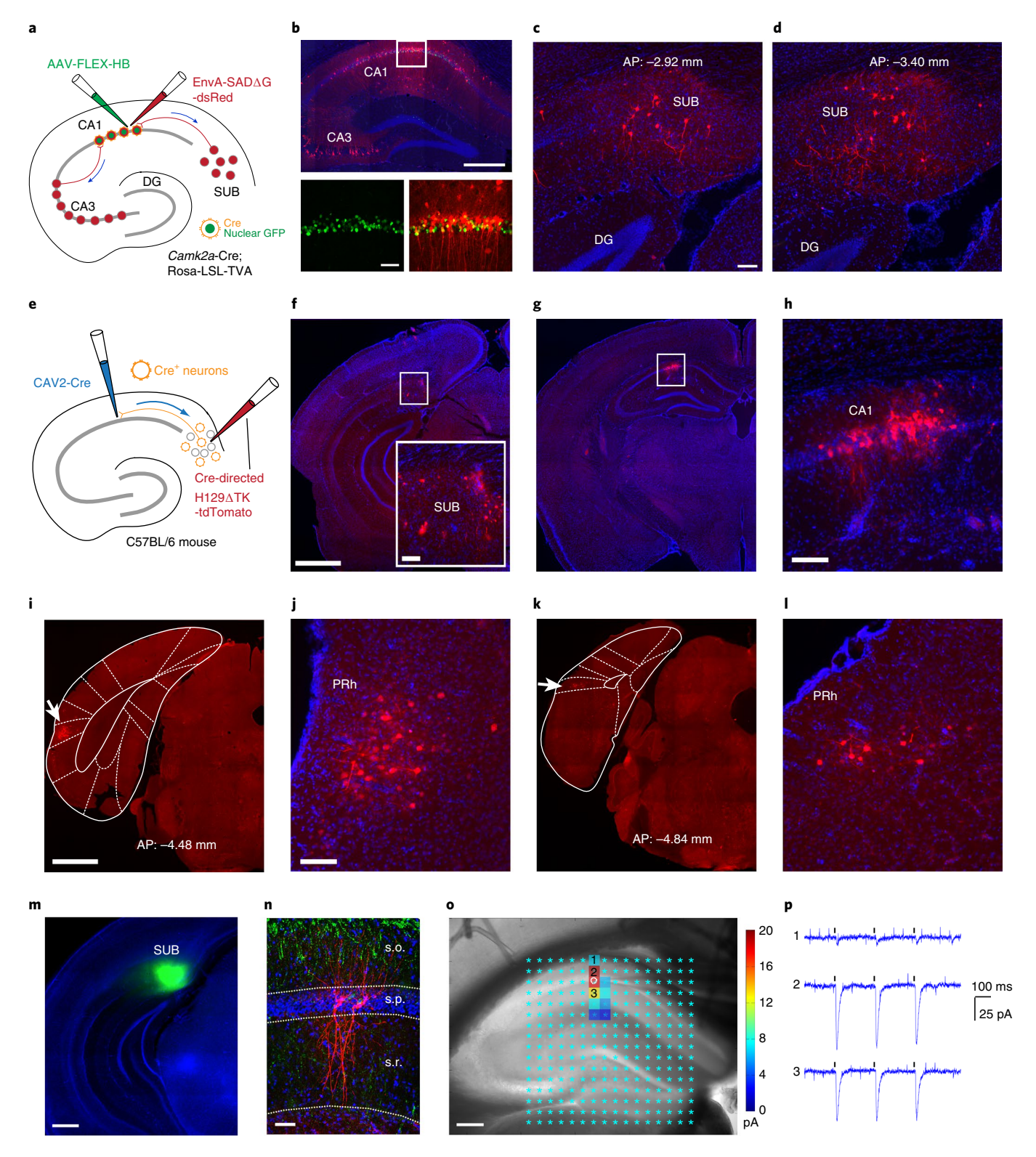
The neurophysiological impact of the SUB-CA1 projections was functionally verified via channelrhodopsin-2 (ChR2)-assisted circuit mapping (CRACM)¹⁶ of SUB-CA1 projections (Fig. 1m-p). Adeno-associated virus (AAV) expressing ChR2 was injected into the SUB in a spatially restricted manner to express ChR2 in SUB neurons (Fig. 1m). Three weeks after virus injection, the ChR2-Venus-expressing axons were seen across CA1 laminae (Fig. 1n). Using live hippocampal slices for CRACM experiments, whole-cell recordings from CA1 pyramidal neurons (N=8 cells) showed clear excitatory synaptic input responses, with the presence of tetrodotoxin (TTX) and 4-aminopyridine (4-AP), to the local photoactivation of ChR2-expressing SUB axons in the CA1 (Fig. 10,p).

Complementing the unique efferent circuitry of SUB neurons projecting to the CA1, we observed that their afferents were also unique in composition (Fig. 2). Afferents to CA1-projecting SUB neurons were mapped and compared with the larger population of excitatory SUB neurons genetically defined by Camk2a-Cre expression¹⁷ (Fig. 2a-o). We employed Cre-dependent monosynaptic rabies virus tracing4 and CAV2-mediated retrograde Cre expression to selectively reveal sources of afferents to CA1-projecting SUB neurons in wild-type (C57BL/6) mice. Both Camk2a-Credefined and CA1-projecting SUB excitatory neurons received the majority of their inputs from the CA1, but differed quantitatively in this respect, as assessed by comparing the CSI values and the percentage of total labeled neurons providing extrinsic inputs to the SUB (Fig. 2p; Supplementary Table 1). CA1 excitatory neuronal input to the SUB accounted for $86.7 \pm 1.6\%$ versus $60.3 \pm 4.4\%$ of the total inputs, respectively, to the excitatory SUB neurons in Camk2a-Cre mice (N=5 cases) and CA1-projecting excitatory SUB neurons selectively labeled by CAV2-Cre (N=6 cases) (P=0.0006;

Fig. 1| The corticohippocampal circuitry involving a non-canonical SUB-CA1 pathway is identified anatomically by retrograde monosynaptic rabies virus tracing and anterograde H129 virus tracing, and verified functionally by ChR2-assisted circuit mapping. a-d, Direct SUB-CA1 backprojections are shown by monosynaptic retrograde rabies virus tracing. This experiment was independently repeated in 12 mice, with similar results obtained each time. a, The scheme for our Cre-dependent, monosynaptic rabies virus tracing approach (for details, see the Methods). Using Camk2a-Cre;TVA mice, we mapped direct presynaptic input connections onto Camk2a-Cre expressing excitatory neurons in the hippocampal CA1 in the intact brain. DG, dentate gyrus. b, Starter neurons in the dorsal hippocampal CA1 are shown (top), labeled by both EGFP and dsRed expression from both AAV and rabies virus infection (bottom). Their presynaptic partners (for example, local interneurons and CA3 neurons) are labeled by the red fluorescent protein dsRed from rabies virus infection. Scale bars, 500 μm (top); 50 μm (bottom). c,d, Retrogradely labeled subicular neurons presynaptic to CA1 excitatory neurons are seen in sections of dorsal SUB at different AP positions: AP: -2.92 mm (c) and AP: -3.40 mm (d). Scale bar, 50 µm. e-h, Time-limited anterogradedirected HSV tracing supports SUB-CA1 projections. This experiment was independently repeated in five mice, with similar results obtained each time. e, The scheme for anterograde tracing by the combined use of CAV2-Cre injection in the CA1 and the injection of Cre-dependent H129 (H129 Δ TKtdTomato) in the SUB to map projections of CA1-projecting SUB excitatory neurons. f, H129-infected neurons at the injection site in the SUB are shown in red; DAPI staining in blue. Scale bars, 1 mm for f and g (inset in f, 200 µm), g,h, Postsynaptic neuronal labeling is robustly seen in the hippocampal CA1 ipsilaterally at 48 h after H129 viral injection. The image in h is the magnified image of the boxed area in g. Scale bar, 200 µm in h. i-l., Besides the CA1, postsynaptic neuronal labeling by H129 is seen in the perirhinal cortex (PRh) ipsilaterally. This experiment was independently repeated in five mice, with similar results obtained each time. i, An example of perirhinal labeling, with a white arrow pointing to the atlas-aligned brain structure of the PRh. The scale bar (1mm) applies to both i and k. j, An enlarged view of the perirhinal neuronal labeling in i. The scale bar (200 μm) applies to both j and I. k, I, Perirhinal labeling, as in i and j, but from a different animal. m-p, Physiological mapping indicates that CA1 pyramidal neurons receive excitatory subicular inputs. This experiment was independently repeated in eight cells from five mice, with similar results obtained each time. m, Spatially localized iontophoretic injection of AAV1-ChR2-Venus in the SUB (green). Scale bar, 500 µm. n, Post hoc verification of biocytin-filled recorded pyramidal neurons (red) along with the distribution of ChR2-Venus-expressing subicular axons (green) counterstained with DAPI in a hippocampal slice. s.o., stratum oriens; s.p., stratum pyramidale; s.r., stratum radiatum. Scale bar, 50 µm. o,p, Direct subicular innervation of CA1 excitatory neurons is shown by postsynaptic current responses to local photoactivation of ChR2-expressing subicular axons in the presence of TTX and 4-AP, which block Na⁺ channels required for generating axonal action potentials and K⁺ channels critical for axonal membrane potential repolarization, respectively. o, Highly localized excitatory subicular inputs impinged onto the recorded excitatory pyramidal neuron (indicated by the white circle). The photoactivation sites (light cyan asterisks) are superimposed on the slice image, with the strength of evoked input sites scored with a color-coded heatmap for average integrated input strength within the analysis window (10 ms to 160 ms post photostimulation), with the baseline spontaneous responses subtracted from the photostimulation response of the same site (for more details, see Methods). Scale bar, 200 µm. p, Raw ChR2 photoactivation responses recorded from the pyramidal neuron in response to three repeated laser flashes (473 nm, 1ms) at the oriens (1), pyramidale (2) and radiatum (3) layer of the CA1.

Supplementary Table 1). The CSI values of CA1 excitatory inputs to Camk2a-Cre and CA1-projecting excitatory SUB neurons differed significantly, with values of 47.72 ± 2.69 versus 14.9 ± 1.25 , respectively ($P=9.13\times10^{-7}$; Supplementary Table 1). Although CA1-projecting SUB neurons received less CA1 excitatory input than the Camk2a-Cre labeled population of excitatory SUB neurons, they received a far denser CA1 inhibitory input, particularly from inhibitory neurons in the stratum oriens ($16.2\pm1.6\%$ versus

 $1.6\pm0.4\%$; CSI: 4 ± 0.44 versus 0.9 ± 0.22 ; P=0.0002). Many of these input-mapped CA1 inhibitory neurons exhibited cell body morphology that resembled oriens-lacunosum-moleculare interneurons (Fig. 2d, right panel; Supplementary Fig. 2a, last panel of the second row), and they were immuno-positive for somatostatin (Supplementary Fig. 2a, last panel of the third row). Furthermore, dense axon plexuses in the CA1 stratum lacunosum-moleculare region appeared to come from rabies-labeled CA1 stratum oriens



neurons (Supplementary Fig. 2a, third row). Together, this result supports the idea that some of the rabies-labeled CA1 inhibitory interneurons share local axonal-projection features of the well-known oriens-lacunosum-moleculare interneurons¹⁸. It remains to be determined whether other CA1 stratum oriens neurons also contribute inhibitory inputs to CA1-projecting SUB neurons.

In addition to the differences in CA1 excitatory and inhibitory inputs, CA1-projecting SUB excitatory neurons received much greater input from the visual cortex and weaker input from the presubiculum. These neurons also received inputs from the retrosplenial granular cortex (RSG). In further contrast to the *Camk2a*-Cre-defined population of SUB excitatory neurons (Fig. 2h-p), CA1-projecting SUB neurons received no input from the temporal association cortex, the perirhinal cortex, the ectorhinal cortex or the EC (Fig. 2a-g,p; Supplementary Table 1). The overall population of excitatory SUB neurons received substantial input from these regions, as reported in prior work^{6,7,19}.

Thus, projection-specific anterograde and retrograde tracing techniques revealed a unique afferent–efferent circuitry associated with CA1-projecting SUB neurons (Fig. 2q). This SUB–CA1 projection can theoretically be considered as a direct feedback system for CA1 output. At the same time, the connectivity pattern showed previously undisclosed pathways by which cortical information, particularly from the visual cortex, can reach and affect activity in the CA1. Prior concepts have most often considered the EC as the primary or even sole integrator of cortical input to the hippocampal system (Fig. 2r).

The direct path from the visual cortex to CA1-projecting SUB neurons and their output to the CA1 and perirhinal cortex strongly suggest that one of the roles for this circuitry may be to provide critical information necessary for conjunctive object–place representations in the hippocampus and the perirhinal cortex. To test this, we used DREADD (designer receptors exclusively activated by designer drugs)-mediated inactivation of CA1-projecting excitatory SUB neurons to determine whether they are necessary for object-location learning behavior (Fig. 3; Supplementary Fig. 3). Inhibitory hM4D DREADD²⁰ were selectively expressed in CA1-projecting SUB neurons using dual CAV2-Cre injection in the CA1 and AAV2-DIO-hM4D-mCherry injection in the SUB of wild-type mice (Fig. 3a,b). Sustained inactivation of CA1-projecting SUB neurons during training was achieved using the hM4D ligand clozapine-

N-oxide (CNO; delivered by systemic injection), and this inactivation was validated by in vitro testing (Fig. 3c; Supplementary Fig. 4a–c).

Compared with mice that received control saline treatment, mice that underwent targeted inactivation of CA1-projecting SUB neurons during the training session displayed much lower object-location discrimination (average discrimination index (DI) of saline treatment: $22.31\pm3.16\%$, average DI of CNO treatment: $4.60\pm2.82\%$; $P\!=\!0.0005$) during the test period when the location of one of the two objects was altered (Fig. 3d; Supplementary Table 2a). This DREADD-mediated inactivation effect was specific to object-location memory (OLM), as additional experiments showed that inactivating CA1-projecting SUB neurons had no effect on investigation of a novel object (Fig. 3e; Supplementary Table 2a).

We next determined whether stimulation of SUB inputs to the CA1 and the perirhinal cortex could enhance OLM. We applied a subthreshold training (3 min) design to test whether optogenetic stimulation at a theta frequency enhances OLM (Fig. 4a,b). Slice electrophysiology experiments showed that ChR2-expressing SUB neurons responded to blue laser stimulation (6 Hz, 50 ms) for 3 min, and remained healthy (as assessed by applying the criteria of the neurons exhibiting stable resting membrane potentials and action potential heights). The majority of the recorded cells faithfully spiked in response to laser stimulation (Fig. 4c,d; Supplementary Fig. 4d-f), thus supporting that there is effective optogenetic stimulation of SUB neurons in vivo under the same stimulation protocol. As expected, control mice (which did not receive laser stimulation) failed to establish memory for object location during the brief training-period exposure and showed no bias to reinvestigation of a relocated object on the subsequent test day (Fig. 4e,f). The same result was obtained in control mice with viral expression of enhanced green fluorescent protein (EGFP) and with laser stimulation applied. In contrast, optogenetic stimulation of CA1-projecting SUB neurons during training led to robust OLM formation; these mice also spent more time investigating the relocated object on the subsequent test day (Fig. 4e,f; Supplementary Table 2b). Thus, there is bidirectional modulation of memory formation through inactivation and stimulation of CA1-projecting SUB neurons.

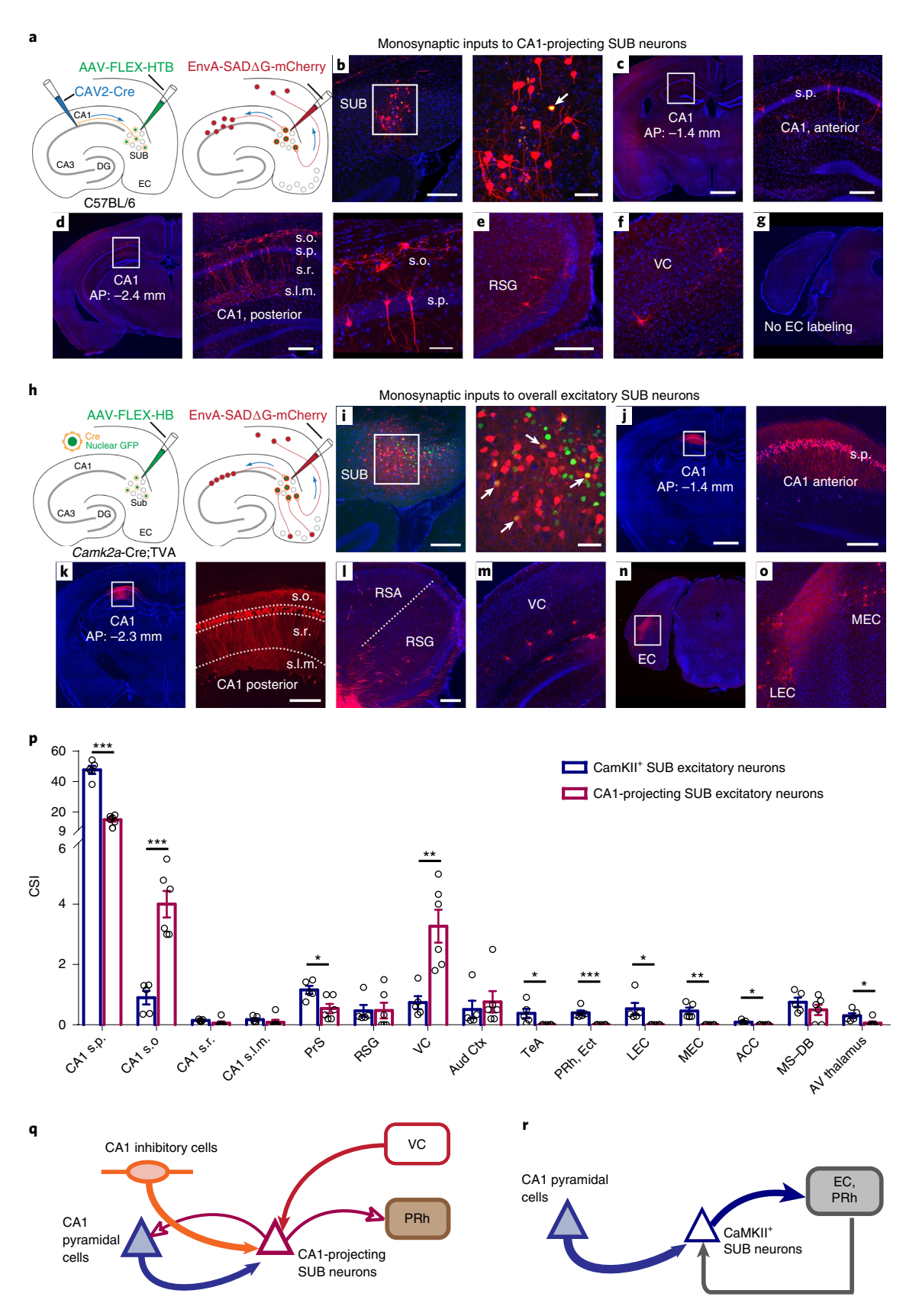
To further characterize the behavioral functions of the SUB-CA1 projection, we examined how DREADD-based inactivation of

Fig. 2 | CA1-projecting SUB excitatory neurons differ in circuit connections from larger populations of SUB excitatory neurons defined by Camk2a-

Cre expression. a-g, Global mapping of input connections to CA1-projecting SUB excitatory neurons using a combinatorial viral genetic tracing method. The approach using CAV2-Cre and Cre-dependent monosynaptic rabies virus tracing is illustrated schematically in a (for details, see Methods). b, The injection site in the SUB. Scale bars, 200 µm and 50 µm, respectively. DAPI staining is blue; rabies-labeled neurons are red. The starter neuron (yellow) indicated by the white arrow appears to receive strong local SUB inputs, as it is surrounded by a cluster of other SUB neurons. c-g, Input-mapped neurons in the dorsal CA1 (c,d), RSG (e) and visual cortex (VC) (f) are also shown, as well as a comparison with no rabies label in entorhinal cortex (EC) (g) (see Supplementary Fig. 2 for more input-mapped regions). CA1-projecting SUB excitatory neurons receive both excitatory and inhibitory CA1 inputs and do not receive direct input from the EC. Scale bars: left panel in **c**, first panel in **d**, and **g**, 1mm; third panel in **d**, 50 μm; all others images, 200 μm; **e** and **f** share the same scale. Note that all the labeled neurons shown in the figure are ipsilateral to the injection site, and very few contralateral labeled neurons were seen across all experimental cases. s.l.m., stratum lacunosum-moleculare. This experiment was independently repeated in six mice, with similar results obtained each time. h-o, Global mapping of input connections to the full population of SUB excitatory neurons using Camk2a-Cre;TVA mice. h, The Cre-dependent monosynaptic rabies virus tracing method is illustrated in the schematics. i, The injection site in the SUB. Scale bars, 200 µm and 50 µm, respectively. DAPI staining is blue; rabies-labeled neurons are red and starter neurons are yellow. j-o, Input-mapped neurons in anterior (AP: -1.4 mm) (j) and posterior (AP: -2.3 mm) (k) dorsal CA1, RSG (I), VC (m) and MEC and LEC (n, o) are also shown (see Supplementary Fig. 2 for more input-mapped regions). Scale bars: j,k left, and n share the same scale, 1mm; all other images, 200 µm. l,m,o share the same scale. This experiment was independently repeated in five mice, with similar results obtained each time. p, Quantitative analysis of input connection strengths of CA1-projecting and Camk2a-Cre SUB excitatory neuron types, showing the CSI for each input-mapped brain structure. Data are measured from Camk2a-Cre expressing SUB excitatory neurons (N=5 cases) and CA1-projecting SUB excitatory neurons (N=6 cases) and are presented as the mean ± s.e.m. Two-tailed t-tests were used to test significance of differences for each input region. Detailed data are provided in Supplementary Table 1b. *P < 0.05, **P < 0.01, ***P < 0.001. ACC, anterior cingular cortex; Au Ctx, auditory cortex; AV, anterior ventral; Ect, ectorhinal cortex; MS-DB, medial septum and diagonal band of Broca, PrS, presubiculum; TeA, temporal association cortex. q.r, Schematics highlighting the major input connections and output projections of CA1-projecting SUB neurons (q) versus CaMKII+ SUB excitatory neurons (r), based on our tracing data shown in Figs. 1 and 2 as well as incorporation of relevant literature on SUB efferent projections. Note that CA1-projecting SUB neurons are GABA immunonegative and 90% of them are CaMKII+ (Supplementary Fig. 1).

CA1-projecting SUB neurons affects mouse performance on a dry-land version of the often-used Morris water maze test²¹ (Supplementary Fig. 5a–d). Temporary inactivation of SUB projections to the CA1 did not impair learning or memory for a spatial location in the dry-land maze task (Supplementary Fig. 5e–j).

Compared with controls, CNO-treated animals exhibited comparable latencies and traveling distances to reach locations flagged by objects. Furthermore, CNO treatment of these same animals did not affect their ability to find a non-flagged spatial target on either the training day or, 24-h later, on the testing day.



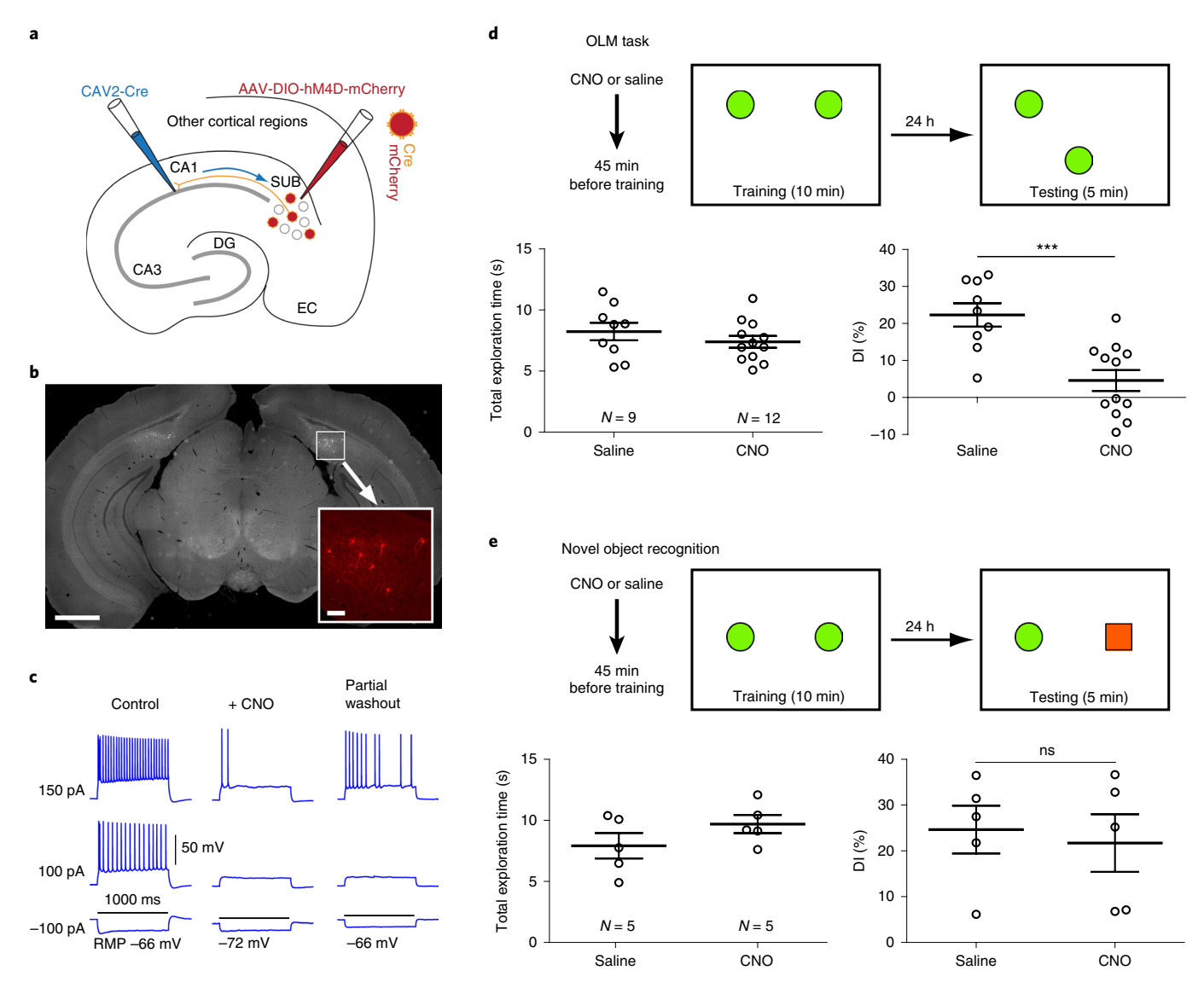


Fig. 3 | Genetically targeted inactivation of CA1-projecting excitatory SUB neurons impairs OLM. a, Schematic illustration of genetic inactivation of CA1projecting SUB excitatory neurons using dual CAV2-Cre injection in the CA1 and AAV2-DIO-hM4D-mCherry injection in the SUB. b, Histological analysis in coronal brain sections verifies bilateral, spatially restricted hM4D-mCherry expression in the SUB. The bottom right inset shows a higher magnification view of the white square region with hM4D-mCherry-expressing CA1-projecting SUB neurons in red. Scale bars, 1 mm and 100 µm (inset). The viral injection experiment was independently repeated in 21 mice, with similar results obtained each time. c, Example electrophysiological data demonstrating in vitro validation of DREADD-mediated SUB neuronal inactivation. CNO (5 µM) application hyperpolarized the resting membrane potential (RMP) of the cell and suppressed action potential firing by intrasomatic current injections. The black horizontal line indicates 1,000 ms of the current injection duration with different strengths (that is, -100 pA, 100 pA and 150 pA). The 5 μM concentration matched the CNO dosage of 1.5 mg per kg used for in vivo DREADD experiments. Given that hM4D is a G-protein-coupled receptor, CNO effects can only be partially reversed with washout of 30-45 min, which is consistent with published results. The experiment was independently repeated in ten cells from four mice, with similar results obtained each time. More validation data are provided in Supplementary Fig. 4a-c. d. Scheme for the experimental design and results of the location-dependent object recognition task following CNO-activated inhibition of CA1-projecting SUB excitatory neurons during the training phase. The box represents the open-field arena, and the green filled circles indicate the training (left) and test (right) object locations. Before the experiment, mice were handled and habituated to the context in the absence of objects. Mice received a single intraperitoneal injection of control saline or experimental CNO treatment (1.4 mg per kg) 45 min before the training. Left: total exploration time of the animals during the testing session. Right: the discrimination index (DI) for the testing session 24h after training. CNO-treated mice did not show a preference for the moved object in contrast to saline-treated controls. Data are presented as the mean ± s.e.m. ***P=0.0005 (two-tailed t-test). e, Test of novel object recognition. In training sessions, two identical objects (green filled circles) were placed in the arena, while for testing, distinct objects (green filled circle and red filled square) were placed in the arena. Mice with inhibition of CA1-projecting SUB neurons showed equal preference for the novel object, similarly to the saline-treated controls. Data are presented as the mean \pm s.e.m. NS, not significant (P=0.73; two-tailed t-test). For more detailed statistics, see Supplementary Table 2a.

The above data indicate that inhibition of CA1-projecting SUB neurons does not impair novel object recognition or navigation to a remembered location defined by distal visual cues. Thus, the

observed impairment in OLM produced by the same manipulation is more likely due to an impairment in connecting objects to their locations in allocentric space. To discern how CA1-projecting SUB

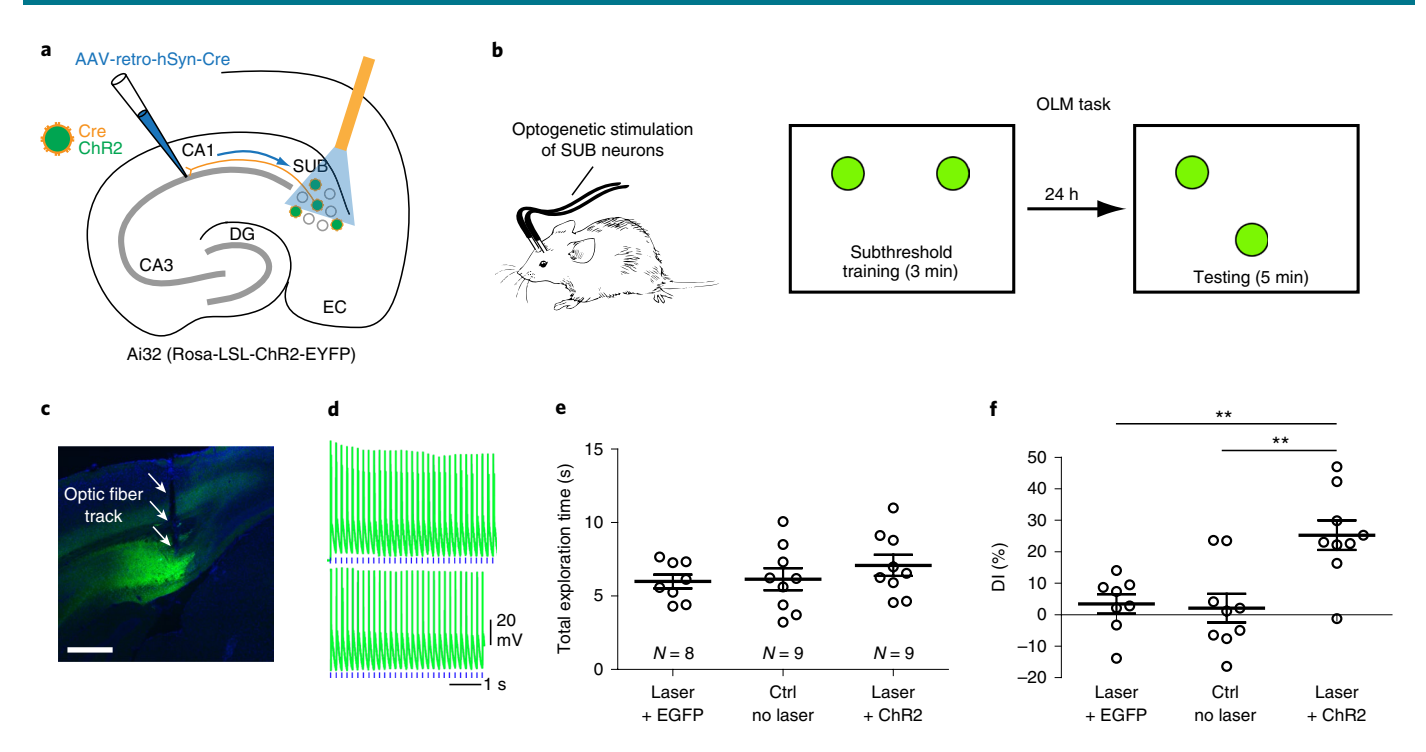


Fig. 4 | Optogenetically activating CA1-projecting SUB neurons enhances OLM. a, Scheme for optogenetic activation of CA1-projecting subicular neurons using AAV-retro-hSyn-Cre in Ai32 (Rosa-LSL-ChR2-EYFP) mice. **b**, Left: schematic depicting a mouse bilaterally connected with optic fibers for delivery of laser stimulation to the SUB. Right: the experimental design of the object-location task for testing the memory enhancement. The box represents the open-field arena and the green filled circles indicate initial and shifted object locations. Object exploration was for only 3 min in training, which normally is subthreshold for long-term memory formation; testing in response to a moved object location following subthreshold training is shown at the far right. **c**, A coronal brain section image showing the expression of ChR2-EYFP (green) in the SUB and an optic fiber track. Scale bar, 200 μm. The viral injection experiment was independently repeated in 18 mice, with similar results obtained each time. **d**, Example responses of a ChR2-expressing SUB neuron to 473 nm blue laser stimulation (6 Hz, 50 ms) for 3 min, with a matched light intensity of in vivo behavioral experiments. Each blue tick beneath the response trace indicates one stimulation. The experiment was independently repeated in 15 cells from 4 mice, with similar results obtained each time. More data are provided in Supplementary Fig. 4d-f. **e**, The total exploration times with objects during the testing session are similar for each condition. **f**, The stable versus displaced object DI during testing for each condition is shown. Mice that received subicular laser stimulation showed strongly increased preference for the moved object in contrast to unstimulated controls or EGFP controls with laser stimulation. Data are presented as the mean ± s.e.m., and a two-tailed *t*-test was used. **P = 0.0018 (top bar) and 0.0027 (bottom bar).

neurons might affect object-location learning, we first examined whether their inactivation affects CA1 encoding of the environmental location of the animal.

We examined the activity patterns of CA1 neuron populations using in vivo GCaMP6-based calcium imaging with miniature fluorescence microscopes^{22,23} (Fig. 5; Supplementary Figs. 6–8). GCaMP6f was selectively expressed in CA1 excitatory neurons via the injection of AAV1-CaMKII-GCaMP6f. Meanwhile, injections of CAV2-Cre into the CA1 and AAV2-DIO-hM4D-mCherry into the SUB of wild-type mice were used to express DREADD in CA1-projecting SUB neurons (Fig. 5a). We tracked calcium transient activity as mice ran along a linear track for a water reward at each end (Fig. 5a-c). Calcium transients in individual CA1 neurons were often localized to one or two locations along a track (Fig. 5d-f), which is consistent with the well-described 'placespecific' action potential firing of CA1 neurons. By identifying the same population of neurons across multiple days (Supplementary Fig. 7a), we were able to compare the location specificity and density of calcium transient activity before, during and after inactivation of CA1-projecting SUB neurons. Three recording sessions, spaced 2-3 days apart, were obtained for each animal (N=6 mice), with the middle recording sessions involving DREADD-based inactivation of CA1-projecting SUB neurons and the first and last serving as pre- and post-DREADD controls (Supplementary Fig. 7b). We also performed three recording sessions under control conditions (*N*=3 mice; Supplementary Fig. 7c) and found stable hippocampal representations across days.

From the CA1 neurons that showed place-specific activity tracked across all three sessions, we examined spatial information, an oftenused metric for place-specific activity²⁴. CNO-induced inactivation of CA1-projecting SUB neurons produced overall reductions in the spatial information metric bits per second (bits s⁻¹; Fig. 5g). No such change in spatial information was seen across multiple control (CNO-free) days in three animals (Supplementary Fig. 8). Furthermore, CNO itself, at our dosage, did not directly affect spatial information or calcium event amplitudes in place cells in control animals²5,26 (Supplementary Fig. 8). In contrast to the observed changes in bits s⁻¹, no CNO-induced changes were observed for the spatial information metric bits per spike (hereafter termed bits per event in keeping with the calcium transient 'events' we imaged; Supplementary Fig. 9).

The contrast between the bits s⁻¹ and bits per event metrics provided a clue to the specific impact of CA1-projecting SUB neurons on CA1 mapping of environmental location. A key difference between the two measures lies in their sensitivity to changes in the magnitude of activity within a place field (as modeled in Supplementary Fig. 9). For simulated firing fields, the bits s⁻¹ metric is sensitive, in a linear fashion, to a wide range of different in-field event rates, while the bits per event metric is not. This suggests that inhibition of CA1-projecting SUB neurons may alter CA1 neuron in-field rates while not affecting event locations.

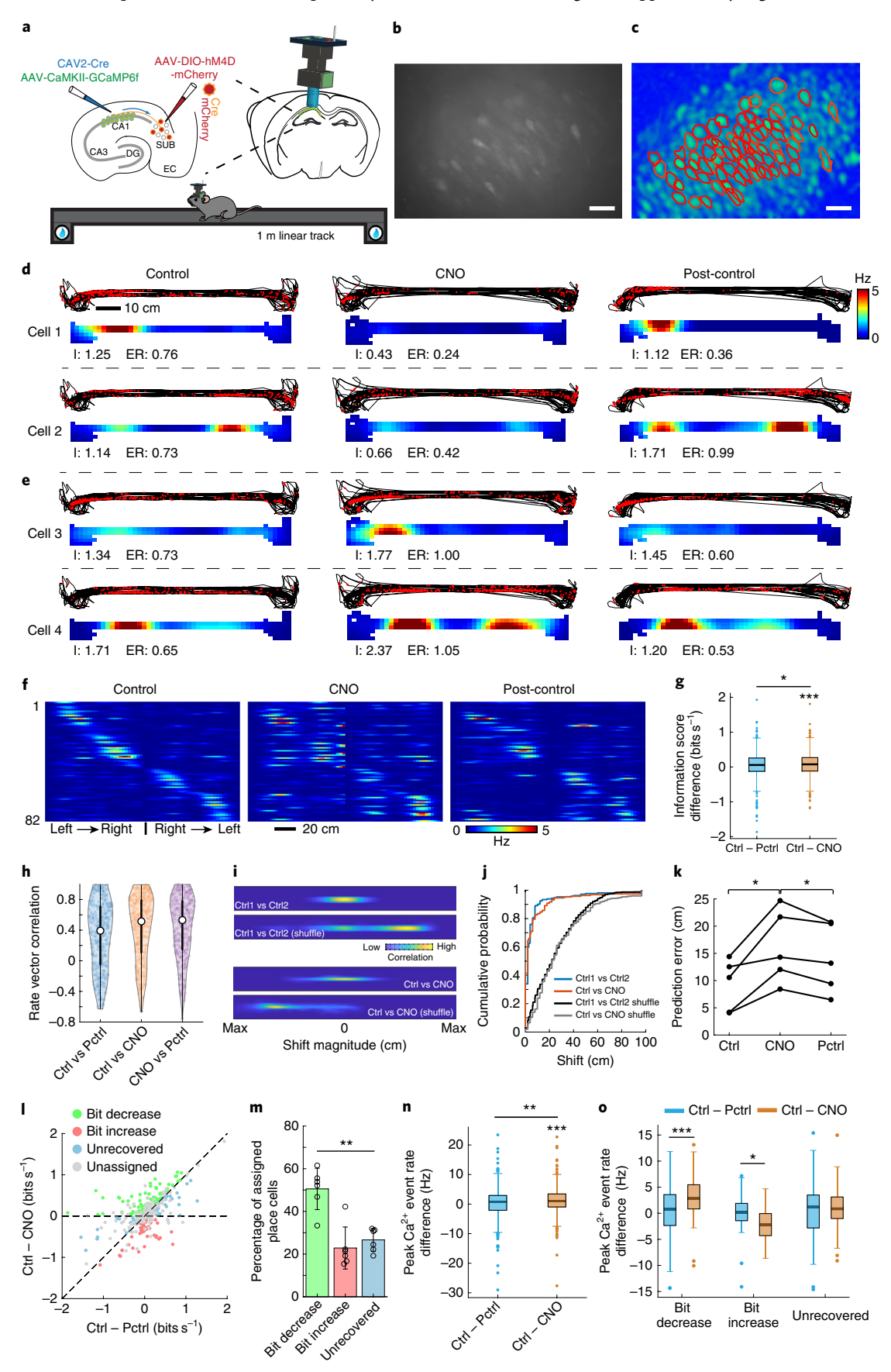
Consistent with the lack of effect of CNO treatment on the bits per event measure, the location-specific patterning of activity among neurons was largely unchanged, as assessed using four different methodologies. First, mean correlations between the positional rate vectors of individual neurons were similar for pairings of control and post-control days to values from either control day paired with testing under CNO (Fig. 5h). This result is inconsistent with either large-scale changes in firing-field locations or the dissolution of place-specific activity itself. Second, ensemble positional

rate vector correlations for odd versus even trial runs and for the first versus second halves of recordings did not vary across control and CNO conditions (Supplementary Fig. 8j-m), thus indicating strong within-session reliability of location-specific activity. Third, direct measurement of field shifts across sessions revealed minimal variation in place-field locations under treatment with CNO versus control sessions (Fig. 5i,j). Actual shifts were far less than one would expect if field locations shifted randomly in response to CNO treatment and were similar to the minimal field shifts seen between

Fig. 5 | CA1-projecting SUB neurons modulate place-specific activity of CA1 neurons in the linear track space. Experiments depicted in the figure were independently repeated in six CNO-treated mice, with similar results obtained each time. For control data, experiments were independently repeated in three mice, with similar results obtained each time. a, Top left: schematic illustration of AAV1 injection for the targeted expression of GCaMP6f in CA1 excitatory neurons and a second dual injection of CAV2-Cre in the CA1 and AAV2-DIO-hM4D in the SUB for targeted expression of DREADD in the CA1projecting SUB excitatory neurons. Top right: schematic depicting a miniaturized fluorescence microscope (miniscope) used to image in vivo calcium signals in CA1 neurons in awake behaving mice. The implanted GRIN lens (shown in blue) and fixed miniscope baseplate allow reliable, repeated imaging of the same group of neurons over 2 weeks. Bottom: cartoon depicting a mouse running on a 1-m linear track during in vivo calcium imaging. Water rewards are placed on both ends of the linear track. b, Representative maximum intensity projected image showing recorded CA1 neurons from three combined 15-min imaging sessions (control, CNO and post-control) across days. The calcium imaging videos were motion-corrected and aligned across sessions. Scale bar, 25 µm. c, A spatial footprint profile image showing extracted neurons (red contours) using the CNMF-E algorithm (see Methods for details) based on the combined video in **b**. Scale bar, 25 µm. **d**, Two sets of panels displaying tracking data (black lines) with superimposed red dots depicting sites where Ca2+ events occurred (top) and corresponding calcium activity rates (bottom) for two example cells (cell 1 and cell 2) from the bit decrease group (see classification below) on the linear track. Each bottom panel is a color-coded rate map showing the averaged spatial distribution of calcium event rates of the same CA1 neuron mapped to the position of the animal on the linear track. Each line shows the event plot and rate maps of control (left), CNO (center) and post-control (right) sessions from the same CA1 place cell over about 2 weeks (2-3 days between sessions). I indicates the spatial information score (bits s⁻¹); ER indicates the mean calcium event rate. **e**, As in **d**, these panels show the activities of two example cells (cell 3 and cell 4) from the bit increase (see classification below) group. f, A color-coded population event-rate map organized by spatial position for left-to-right track traversals and then right-to-left traversals of all place cells from one representative mouse during control, CNO and post-control sessions. The depicted cell order is unchanged across the sessions of control, CNO and post-control as determined initially in the control session. Each line shows the activity of one place cell. Color indicates event rate (scale bar). The overall rate-map correlation values (Pearson's) between control and post-control sessions and between control and CNO sessions are 0.61 and 0.54, respectively, g, Comparison of the difference of spatial information scores (bits s⁻¹) between control and post-control (Ctrl - Pctrl, two-tailed t-test against zero: P = 0.15), and between control and CNO (Ctrl - CNO, two-tailed t-test against zero, ***P=1.3×10⁻⁴) across all 347 place cells recorded from 6 mice. Differences between Ctrl - Pctrl and Ctrl - CNO were also observed (two-tailed, paired t-test, *P = 0.03). **h**, A violin plot showing the distribution of rate vector correlation coefficients (Pearson's) of individual place cells for all session combinations (control versus CNO, control versus post-control, and CNO versus post-control). The median value for control versus post-control, control versus CNO and CNO versus post-control are 0.40, 0.51 and 0.53, respectively (N = 347 place cells from 6 mice). The white open circles indicate median values, and the thin black lines extend to the most extreme values within 1.5 times the IQR of the median. The filled color width represents a density estimate of the distribution of values along the y axis. i, Spatial cross-correlograms of example CA1 cells from the saline-treated experiment (Ctrl1 versus Ctrl2) and CNO-treated experiment (Ctrl versus CNO). Shuffled examples were obtained by randomly pairing rate maps across the same comparison sessions as for the example cells. j, The distributions of correlation-peak shift magnitudes for the place cells in the saline experiment (blue line) and the CNO experiment (red line) differ significantly from the corresponding shuffled distributions ($P = 3.17 \times 10^{-64}$, two-tailed, two-sample Kolmogorov-Smirnov (KS) test, N=174 cells from Ctrl1 versus Ctrl2 and 1,000 shuffles from Ctrl1 versus Ctrl2; $P=1.48\times10^{-101}$, two-sample KS test, two-tailed, N=347 cell from Ctrl versus CNO and 1,000 shuffles from Ctrl versus CNO). Shuffled distributions were obtained by randomly pairing place maps 1,000 times across the indicated sessions. There was no significant difference between the distribution of Ctrl versus CNO (red line) and the Ctrl1 versus Ctrl2 (blue line) (P=0.38, two-sample KS test, two-tailed). k, Quantification of the prediction errors between predicted trajectories and actual trajectories for decoding accuracy using the trained model based on the first control session, which supports the observations presented in Supplementary Fig. 8a. Each line represents the prediction errors of control, CNO and post-control sessions from one mouse. Significantly higher prediction errors are observed in CNO sessions compared with those in control ($^*P = 0.016$, two-tailed, paired t-test) and post-control ($^*P = 0.015$, two-tailed, paired t-test) sessions. N = 5 mice. I, Recorded CA1 place cells can be classified into three non-overlapping groups termed bit decrease, bit increase and unrecovered (see Methods for more information about the group classifications), based on the statistical significance of differences in information scores (bits s⁻¹) between CNO and control and between CNO and post-control. Statistical testing employed a jackknife resampling method for each place cell with appropriate corrections for error terms. Unassigned place cells did not pass the statistical test and were excluded from further categorization analysis. On the scatter plot, the x axis is Ctrl - Pctrl (the difference of spatial information scores between control and post-control) and the y axis is Ctrl - CNO (the difference of information scores between control and CNO). m, Of the 201 place cells that showed significant differences (assigned place cells) from 6 mice, 50% showed decreased information scores in CNO sessions compared with the control and post-control sessions (bit decrease group). A smaller subset (~23%) showed increased information scores in CNO compared with the control and post-control (bit increase group). The remaining ones are the unrecovered group, which accounted for ~27% of place cells. Comparing the mean percentages of each type seen in each mouse, a significant difference in the percentage of place cells among these three groups was observed (**P = 0.002, repeated measures ANOVA, N = 6 mice). Data are presented as the mean \pm s.e.m. in the bar plot. **n**, Comparison of the difference of peak calcium event rates between control and post-control (Ctrl - Pctrl, two-tailed *t*-test against zero, *P* = 0.32) and between control and CNO (Ctrl - CNO, two-tailed t-test against zero, ***P=1.6 × 10⁻⁵) across all 347 place cells recorded from 6 mice. Differences between Ctrl - Pctrl and Ctrl - CNO were also observed (two-tailed, paired t-test, **P=0.004). o, Comparisons of peak calcium event rates between Ctrl - Pctrl and Ctrl - CNO in bit decrease (two-tailed, paired t-test, *** $P=3\times10^{-7}$, N=97 cells), bit increase (two-tailed, paired t-test, *P=0.027, N=48cells) and unrecovered groups (two-tailed, paired t-test, P=0.20, N=56 cells). For all the box plots in this figure, the three box lines from top to bottom represent the 25th, 50th (median) and 75th percentiles of data values of the samples. The whiskers extend to the most extreme values within 1.5 times the IQR of the median.

control sessions. Fourth, using an artificial neural network to decode the position of the animal in the second and third recording sessions (that is, CNO and post-control sessions, respectively) based

on a trained model from the first control session, we found only slightly reduced decoding accuracy in the CNO versus post-control session (Fig. 5k; Supplementary Fig. 8a). Thus, changes in the



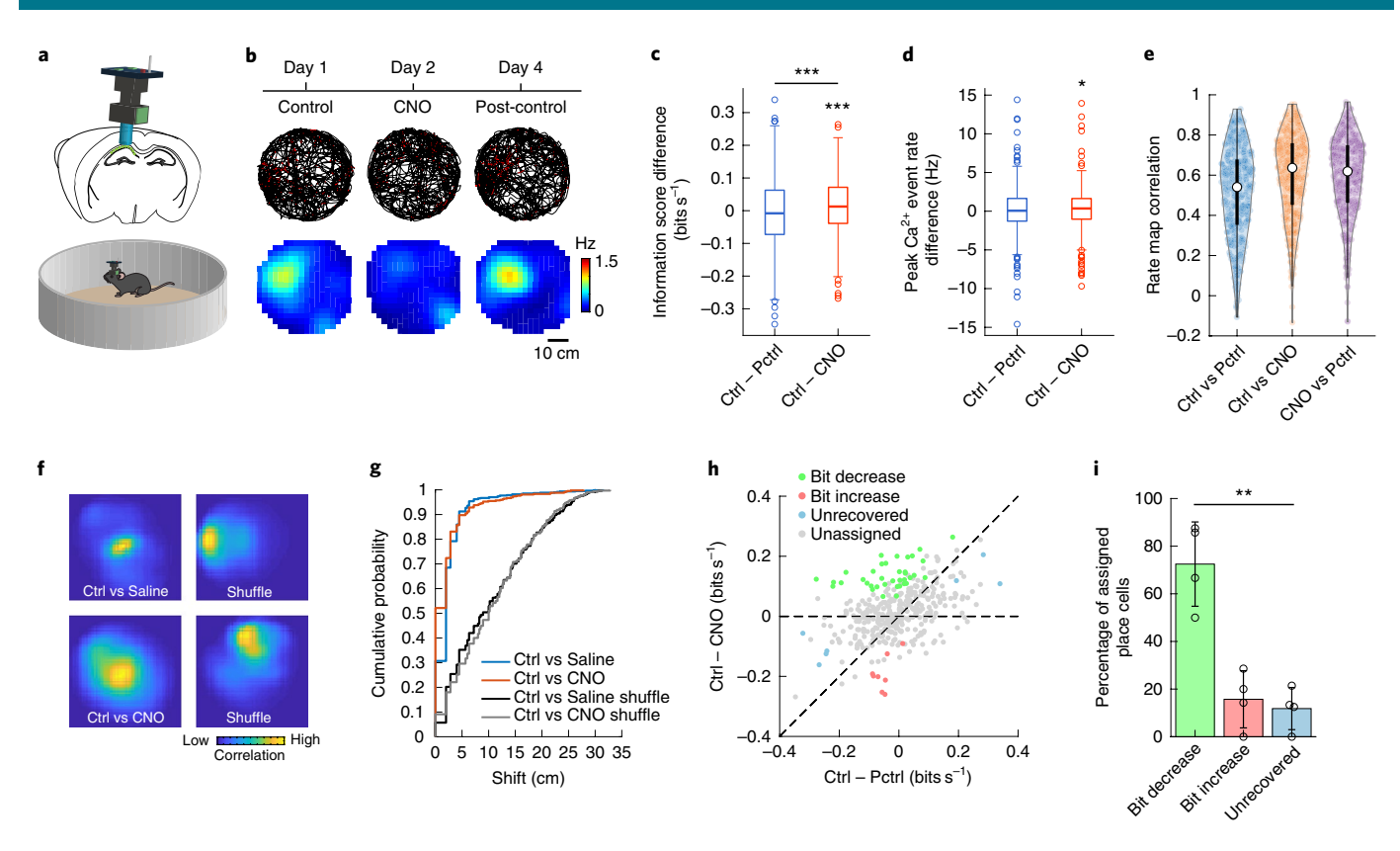


Fig. 6 | Inactivation of CA1-projecting SUB neurons affects CA1 neural activities in an open field. A cohort of mice with bilateral hM4D expression in CA1-projecting SUB neurons were used for these experiments. Miniscope imaging of CA1 place cell activities were obtained while animals explored an open arena. The experiments were independently repeated in four mice per treatment group, with similar results obtained each time. a, A schematic illustration of the CA1 Ca^{2+} imaging experiment in a circular arena. **b**, Top: example position sampling (gray lines) and locations of Ca^{2+} events of a single neuron (red dots) for control, CNO and post-control sessions. Bottom: calcium event-rate maps for the same example cell across sessions. The experimental time line is shown above. c, Comparisons of the difference of spatial information score (bits s-1) between control and post-control (Ctrl - Pctrl, two-tailed t-test against zero: P = 0.26), and between control and CNO (Ctrl - CNO, two-tailed t-test against zero, *** $P = 1.82 \times 10^{-4}$) across 379 place cells from 4 mice. Significant differences between Ctrl - Pctrl and Ctrl - CNO were also observed (two-tailed, paired t-test, ***P = 2.73 × 10⁻⁵). For all the box plots in this figure, the three box lines from top to bottom represent the 25th, 50th (median) and 75th percentiles of data values of the samples. The whiskers extend to the most extreme values within 1.5 times the IQR of the median. d, Comparisons of the difference of peak calcium event rates of individual place cells between control and post-control (Ctrl - Pctrl, two-tailed t-test against zero, P = 0.32), and between control and CNO (Ctrl - CNO, two-tailed t-test against zero, *P=0.02). **e**, A violin plot showing the distribution of rate-map correlation coefficients (Pearson's) of individual place cells for all session combinations. The median values for control verus post-control, control versus CNO, and CNO versus post-control are 0.51, 0.60 and 0.59, respectively (N = 379 place cells from 4 mice). The overall high correlation indicates consistent and stable positional coding between different conditions. In the violin plot, the open white circles indicate median values, and thin black lines extend to the most extreme values within 1.5 times the IQR of the median. The filled color width represents a density estimate of the distribution of values along the y axis. f, Spatial cross-correlograms of example CA1 cells from the saline-treatment experiment (Ctrl vs Saline) and CNO-treatment experiment (Ctrl vs CNO). Shuffled examples were obtained by randomly pairing place maps across the same comparison sessions as for the example cells. g, The distributions of correlation-peak shift magnitudes for the place cells in the saline experiment (blue line) and the CNO experiment (red line) differ significantly from the corresponding shuffled distributions $(P=1.94\times10^{-107}, \text{two-sample KS test, two-tailed}, N=606 \text{ place cells from Ctrl vs Saline and 1,000 shuffles from Ctrl vs Saline; } P=2.05\times10^{-97}, \text{two-sample KS test, two-tailed}, N=606 \text{ place cells from Ctrl vs Saline and 1,000 shuffles from Ctrl vs Saline; } P=2.05\times10^{-97}, \text{two-sample KS test, two-tailed}, N=606 \text{ place cells from Ctrl vs Saline and 1,000 shuffles from Ctrl vs Saline; } P=2.05\times10^{-97}, \text{two-sample KS test, two-tailed}, N=606 \text{ place cells from Ctrl vs Saline}, P=2.05\times10^{-97}, \text{two-sample KS test, two-tailed}, N=606 \text{ place cells from Ctrl vs Saline}, P=2.05\times10^{-97}, \text{two-sample KS test, two-tailed}, N=606 \text{ place cells from Ctrl vs Saline}, P=2.05\times10^{-97}, \text{two-sample KS test, two-tailed}, N=606 \text{ place cells from Ctrl vs Saline}, P=2.05\times10^{-97}, \text{two-sample}, P=2.05\times10$ KS test, two-tailed, N = 379 place cells from Ctrl vs CNO and 1,000 shuffles from Ctrl vs CNO). Shuffled distributions were obtained by randomly pairing place maps 1,000 times across the indicated sessions. The distribution of control versus CNO (red line) is slightly left shifted compared with control versus saline (blue line) ($P=1.69\times10^{-10}$, two-sample KS test, two-tailed). **h**, In the CNO inactivation experiment in the open field, recorded CA1 place cells were classified into three non-overlapping groups termed bit decrease, bit increase and unrecovered based on the statistical significance of differences in information scores (bits s⁻¹) between CNO and control and between CNO and post-control subject to a jackknife resampling test for each place cell. Unassigned place cells did not pass the statistical test with jackknife resampling and were excluded from further categorization analysis. On the scatter plot, the x axis is Ctrl - Pctrl (the difference of spatial information scores between control and post-control) and the y axis is Ctrl - CNO (the difference of information scores between control and CNO). i, Of the 52 place cells that passed the statistical test from 4 mice, on average, 72% showed decreased information scores in CNO sessions compared with the control and post-control sessions (bit decrease group). A smaller subset (16%) showed increased information scores in CNO compared with the control and post-control (bit increase group), and the remaining 12% belonged to the unrecovered group. There was a significant difference across the group percentage values (**P=0.0033, repeated measures ANOVA, N=4 mice), while the saline control experiment did not show this difference (Supplementary Fig. 10f). Data are presented as the mean \pm s.e.m. in the bar plots.

locations of place-specific activity are much smaller than one might expect if the place specific activity of CA1 neurons had undergone complete or 'global' remapping'²⁷, wherein the firing-

field locations of individual neurons vary randomly across sessions. These results are also incompatible with a general dissolution of place-specific activity.

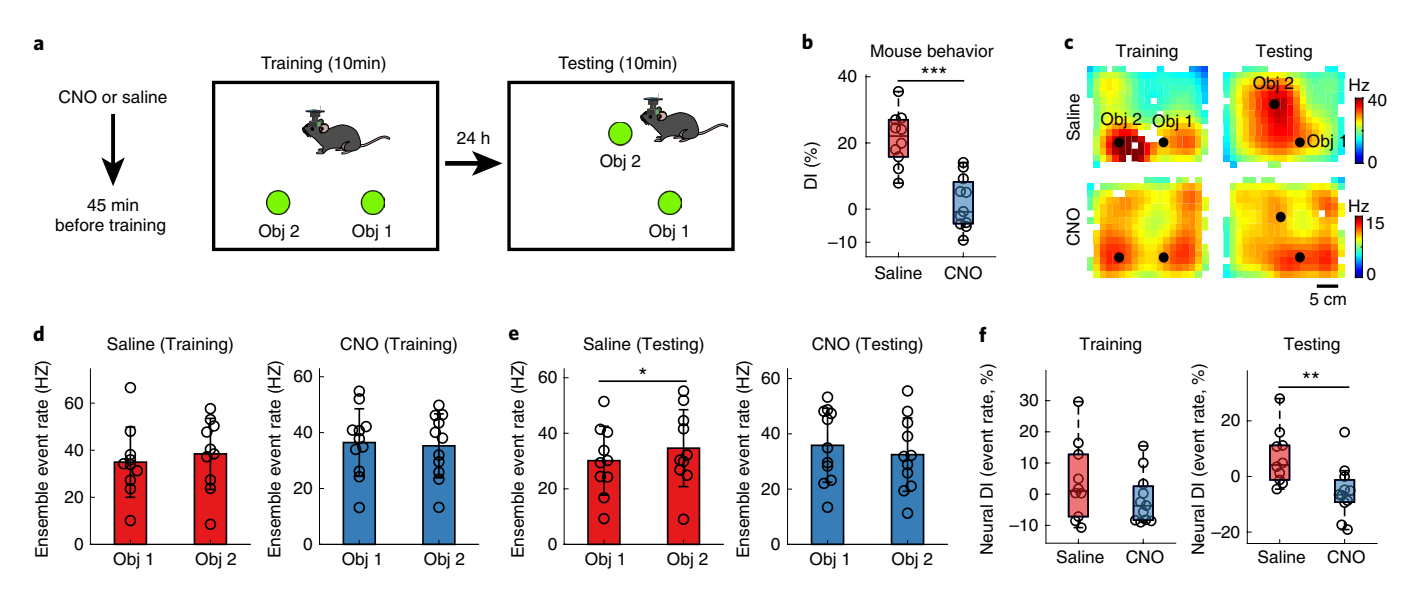


Fig. 7 | Inactivation of CA1-projecting SUB neurons modulates CA1 neural activity correlated with impaired OLM performance. a, Schematic of the task and timeline. Obj, object. **b,** CNO-treated mice (N=11) exhibited significantly impaired OLM performance compared with saline-treated controls (N=10), as reflected in the lower DI (two-tailed Welch's t-test, *** $P=2\times10^{-5}$). **c,** Ensemble Ca²+ event-rate maps of all cells during training and testing phases from one saline-treated control mouse (343 cells) and one CNO-treated mouse (182 cells). The ensemble event rates are the summation of events from all recorded neurons normalized by time spent at each location. **d,** No significant differences of ensemble Ca^{2+} event rates between the two objects for both saline-treated control mice (N=10, P=0.274) and CNO-treated mice (N=11, P=0.576) were seen during the OLM training phase. P values are from two-tailed paired t-tests. **e,** Ensemble Ca^{2+} event rates during the OLM testing phase. We observed significantly higher Ca^{2+} event rates around the displaced object (object 2) compared with that around the stable object (object 1) for saline-treated control mice (N=10, *P=0.032). There was no difference of Ca^{2+} event rates around object 2 versus object 1 for CNO-treated mice (N=11, P=0.14). P values are from two-tailed paired t-tests. **f,** CNO-treated mice (N=11) did not differ from saline-treated control mice (N=10) in terms of the neural DI calculated with ensemble Ca^{2+} event rates during the training session (P=0.244, two-tailed Welch's t-test), but showed decreased neural discrimination during the testing session (*P=0.0099, two-tailed Welch's t-test). This neural DI is based on relative event rates and expressed as ($ER_{object2}-ER_{object1}$)/($ER_{object1}$) × 100%, wherein $ER_{object2}$ and $ER_{object2}$ are the ensemble event rates associated with the two objects, respectively. For all the box plots in this figure, the three box lines from top

An alternative form of modulation in spatially specific activity is termed 'rate-remapping', wherein in-field activity rates of CA1 place cells are altered despite no change in the locations of spatially specific activity²⁷. Such positive and negative modulations of in-field place-specific firing allows hippocampal place cells to encode both locations and the context associated with being in those locations. Because the observed changes in the bits s⁻¹ metric for CA1 place-specific activity is more compatible with this form of remapping, we next examined the possibility that inactivation of CA1-projecting SUB neurons affects in-field firing.

To organize our analysis of rate remapping, we segregated neurons according to their individual positive or negative changes in cross-session spatial information scores (bits s⁻¹). For each neuron, we examined whether its spatial information score in the CNO session was significantly different from that in both the control and post-control sessions using a jackknife resampling method²⁸. Each track-running session was divided into ten equal-duration subsessions. We then applied the jackknife resampling to the full recording session, each time calculating bits s-1 values based on nine out of the ten subsessions. The now extended sets of bits s-1 values produced by this resampling procedure were then subjected to statistical testing (see Methods for details). A place cell was classified as 'bit decrease' only when its spatial information in the CNO session was significantly lower than in both the control and post-control sessions. A 'bit increase' neuron exhibited a CNO-session bits s-1 value that was higher than that of each control session. A place cell that passed the statistical test in the CNO versus control and the CNO versus post-control comparisons, but with opposite directions of change, was classified into the 'unrecovered' group. The remainder

of the place cells, which failed at least one of the statistical tests, were unassigned and excluded from the category analysis.

Among the 201 place cells (from 6 mice) showing significant differences in CNO versus control and CNO versus post-control sessions, we found 73% that exhibited either information decreases (bit decrease group, 50%) or information increases (bit increase group, 23%) relative to both control and post-control sessions (Fig. 5l,m). The remainder (27%), were characterized as unrecovered, showing non-uniform changes in spatial information in CNO versus control sessions. The number of neurons falling into the bit decrease category was equal to the combined number of cells in the bit increase and unrecovered categories, a bias that was consistent with the overall decrease in bits s⁻¹ (Fig. 5g). Furthermore, this bias was reliable across animals (Fig. 5m). Finally, in 174 place cells recorded under three consecutive control sessions (Supplementary Fig. 7c), we did not observe significant changes in spatial information for the second session (Supplementary Fig. 8d). The percentage of assigned place cells characterized as bit decrease in the second control session relative to the first and third control sessions was not significantly greater than that of the bit increase or unrecovered category, and it was significantly lower than that in CNO-treated animals (Supplementary Fig. 8c,f,g).

Thus, by using several measures, we showed that inactivation of CA1-projecting SUB neurons minimally affects the locations at which individual CA1 neurons are highly active. Yet, there was an overall significant bias toward reduction in the bits s⁻¹ spatial information metric at both the population-level and single-neuron-level analysis. The former result indicates that the latter is likely not explained by an increased scattering of calcium events across track

space, but instead reflects changes in the peak in-field magnitude of location-specific activity. Consistent with this notion, we found that peak in-field calcium event rates exhibited a similar pattern with bits s⁻¹ changes across the control, CNO and post-control sessions. Overall peak event-rate differences were seen when comparing the CNO to control session, but not in comparing the post-control to control session (Fig. 5n). No peak event-rate differences were observed in the three consecutive control sessions (Supplementary Fig. 8h). As expected, based on the sensitivity of the bits s⁻¹ metric to event rates (Supplementary Fig. 9e,f), the neuron subpopulation exhibiting significant decreases in bits s-1 values under CNO treatment was, overall, observed to have significantly reduced peak activity rates (Fig. 50). The subpopulation with spatial information increases exhibited rate increases (Fig. 50). Together, these findings provide evidence of reliable alterations in the magnitude of location-specific activity in CA1 neurons subsequent to DREADDbased inactivation of their SUB inputs. CA1-projecting SUB neurons can therefore be considered to contribute to the peak in-field event rates of CA1 neurons under control conditions. Their inhibition induces a form of 'rate-remapping' in CA1 with a bias toward reduced in-field activity.

We further characterized the impact of inactivation of the SUB–CA1 back-projection on CA1 neural activity during open-field exploratory behavior using a separate cohort of mice (Fig. 6; Supplementary Fig. 10). As on the linear track, DREADD-based inactivation of CA1-projecting SUB neurons reduced the bits s⁻¹, but not bits per event, spatial information scores among CA1 place cells (Fig. 6c; Supplementary Fig. 9c,d). Overall peak in-field firing was depressed under CNO compared with control conditions, but differences in control versus post-control values were not observed (Fig. 6d). In close agreement with the data obtained during track running, CNO did not significantly change the locations of CA1 place fields, as assessed through cross-session correlation of event-rate maps and direct measurement of field shifts (Fig. 6e–g; Supplementary Fig. 10a–d).

Further replication of the open-field-based data was observed when information changes in individual neurons were assessed in the category analysis using the jackknife resampling approach. Of the 52 assigned place cells, we consistently observed a bias toward larger numbers of neurons that exhibit significant information decreases (72%; Fig. 6h,i). Thus, more than three times as many place cells fall into the bit decrease (lower bits s⁻¹) than the bit increase (16%) or unrecovered (12%) category. This bias was not seen in the control animal group (Supplementary Fig. 10e–g).

To more directly assess the contribution of SUB projections to the CA1 on OLM, we also conducted miniscope imaging experiments in behaving mice during the OLM task itself (Fig. 7a). In this cohort of mice, we again observed impairment in OLM following inactivation of CA1-projecting SUB neurons (Fig. 7b). DREADD-based inactivation of this subgroup of SUB neurons during the training session led to significant impairment in long-term location-dependent memory, as assessed on the subsequent testing day. Similar to the original cohort of animals undergoing this test (Fig. 3d), saline controls spent significantly more time interacting with the newly displaced object than with the unmoved object, while overall CNO-treated animals spent the same amount of time interacting with each object (Fig. 7a,b; Supplementary Table 3).

To determine whether neural responses to object displacement parallel behavioral responses, we generated ensemble-wide Ca²⁺ event-rate maps of CA1 neurons for each recording (Fig. 7c). The ensemble event rates are the summation of events from all recorded neurons normalized by the time spent at each location. We did not observe significant differences in the ensemble-wide rate of Ca²⁺ events at the two object locations during training sessions for either saline-control mice or CNO-treated mice (Fig. 7d). However, for control mice, displacement of one object on the testing day

produced a small but significant increase in CA1 activity at the site of that object compared with the unmoved object (P = 0.032; Fig. 7e). In contrast, there was no such difference in Ca²⁺ event rates in CNO-treated mice. The event-rate values at the displaced and unmoved object positions were compared using the neural discrimination index (neural DI) presented in Fig. 7f. For each animal, the ensemble-wide event-rate DI was calculated as follows: (event rate at object 2 – event rate at object 1)/(event rate at object 2 + event rate at object 1)×100%. The average DI was positive for saline-treated animals, indicating that there were enhanced neural responses to the displaced object, but slightly negative for CNO-treated animals, indicating that there was weak discrimination of the two objects. This effect was significant for up to a 3-cm space surrounding each object (Supplementary Fig. 10h). Thus, DREADD-based inactivation of CA1-projecting SUB neurons significantly reduces the discrimination in activity levels at the relocated versus stable object (P=0.005; Fig. 7f). To further test the specific contributions of place cells in the object-location experiment, for each animal, we determined the ratio of place-cell fields (see Methods for details) in relation to each object and compared these ratios for the salinetreated group and CNO-treated group. Example neuron event-rate maps are shown in Supplementary Fig. 10i-j. Both saline-treated and CNO-treated groups exhibited roughly the same number of fields for both objects during the training session (Supplementary Fig. 10k). We found a significant difference in these ratios, with higher numbers of place fields associated with the displaced object for the saline-treated group and lower numbers of place fields related to the displaced object in the CNO-treated group during the testing session (Supplementary Fig. 10l). Together, these results parallel the changes observed in behavioral discrimination. Targeted inactivation of the SUB-CA1 back-projection pathway during OLM training affects ensemble neural activity associated with long-term object-location-dependent memory.

Discussion

In this work, we identified a distinct subpopulation of SUB neurons forming a pathway from the visual cortex to the CA1 and the perirhinal cortex, and demonstrated that this pathway plays a critical role in object-location learning and memory. We refer to this circuit as non-canonical in that it runs opposite to the feedforward pathway leading from the CA1 to the SUB and the retrosplenial cortex. CA1-projecting SUB neurons are simultaneously poised to act in a feedback loop to the CA1 and in a pathway for visual information to directly affect the two major output structures of the hippocampus: the CA1 and the SUB. By combining trans-synaptic viral-tracing techniques, in vivo GCaMP6-based calcium imaging, projection-specific manipulations and behavioral testing, the present set of experiments revealed the presence of a cortico-hippocampal circuit that affects specific learning and memory behaviors.

The unique afferent–efferent circuitry of CA1-projecting SUB neurons and their bidirectional modulation of CA1 in-field activity rates is consistent with the previously observed roles of CA1 neurons in the formation of OLM. It is now established that a small population of CA1 neurons exhibit 'landmark vector' responses that reflect the location of the animal relative to objects²⁹. Thus, one of the roles for visual cortex inputs to CA1-projecting SUB neurons may be to provide a direct avenue by which information concerning the visual presence of objects is directly routed to the CA1 for integration with neurons that encode current environmental location. Here, it is notable that some neurons of the rat visual cortex exhibit reliable position-specific firing rates during track running, which is consistent with the encoding of position-specific visual experience³⁰.

Precisely how CA1-projecting SUB neurons mediate OLM at the level of synapses remains to be determined. Their inactivation does not affect navigation according to distal visual boundary cues in an

object-free environment (see our dry-land experiments), a result consistent with the largely unchanged locations of place-field activities under the same manipulation. The larger effect on CA1 dynamics was found to be on peak in-field calcium event rates. During inactivation of CA1-projecting SUB neurons, weaker responses for a majority of CA1 neurons were observed. Inactivation during initial exposure to two objects in an open field led to a subsequent failure of CA1 populations to generate stronger responses to spatially displaced objects. This result implies that OLM formation fails when CA1 neurons cannot integrate place-specific responses with the inputs of CA1-projecting SUB neurons.

The afferent circuitry of CA1-projecting SUB neurons includes the retrosplenial cortex, which encodes conjunctions among multiple types of spatial information^{31,32} and is required when visual cues are flexibly used to determine location³³. Under conditions of associative learning of visual stimuli, the retrosplenial cortex is a prominent contributor to activity patterns observed in visual cortex regions that project to the SUB³⁴. Therefore, the retrosplenial cortex could influence the SUB and the CA1 through direct connections and indirectly through the visual cortex.

Compared with the full population of excitatory SUB neurons, CA1-projecting SUB neurons receive especially dense input from CA1 inhibitory neurons. This projection is mainly from inhibitory neurons in the stratum oriens. Many of these neurons also send efferents to the CA1 stratum lacunosum-moleculare, similar to the projection pattern of some somatostatin-expressing stratum oriens neurons^{18,35}. This aspect of the anatomical data is remarkable considering several parallel features of hippocampal and rhinal cortex anatomy and physiology. First, CA1-projecting SUB neurons also project to the perirhinal cortex, a structure providing extensive input to the lateral EC (LEC)³⁶. Second, recent data indicate that both LEC and medial EC (MEC) neuron subpopulations exhibit distinct responses to objects^{37,38}. Third, somatostatin-expressing CA1 stratum oriens interneuron firing is locked to similar phases of theta-frequency oscillations as for CA1 pyramidal and EC neurons^{18,39}. Fourth, some CA1 stratum oriens neurons innervate distal apical dendrites of CA1 pyramidal neurons receiving LEC and MEC inputs as well as CA1-projecting SUB neurons. Finally, CA1 pyramidal cell inputs to stratum oriens neurons are subject to longterm potentiation⁴⁰. Therefore, CA1 stratum oriens neurons are well positioned to provide learning-dependent feedback regulation that can temporally organize the processing of object-location information across a wide network, including CA1-projecting SUB neurons, the CA1 and the perirhinal cortex and EC.

These fine-scale features of circuitry connecting the SUB, hippocampus, EC and perirhinal cortex are more interesting when considering the results of lesion studies of memory formation and neurophysiological features of the CA1, LEC and perirhinal cortex^{41,42}. Here, we note the opposing and complementary topographic connectivity gradients revealed by our quantitative analysis of canonical and non-canonical hippocampal CA1 inputs; noncanonical SUB inputs co-track the weak-to-strong LEC inputs along the transverse axis of the CA1 (ref. 5). Recent work has revealed extensive encoding of object locations relative to the animal in the LEC³⁸. It follows that, to some degree, such responses to objects are transmitted to CA1 neurons through terminals in the stratum lacunosum moleculare where some somatostatin-expressing stratum oriens interneuron axons also terminate. Furthermore, interactions between the CA1 and the perirhinal cortex are necessary for the development of object-place memory^{41,43,44}, which is now supported by our finding that CA1-projecting SUB neurons also project to the perirhinal cortex.

In light of our circuit-mapping results, it is clear that visual and retrosplenial cortical input can reach the perirhinal cortex through direct projections from CA1-projecting SUB neurons. Like the CA1, perirhinal cortex neurons respond to objects^{42,45}, and lesions

produce impairments in the expression of object-place memory^{15,46}. Bidirectional beta-frequency- and gamma-frequency-paced stimulation of the perirhinal cortex modulates the recognition of objects as familiar versus novel⁴⁷. The perirhinal cortex in turn densely innervates the LEC, and LEC efferents more densely innervate distal regions of the CA1, where SUB-to-CA1 projections are most dense⁵. Notably, subpopulations of LEC neurons exhibit object responses persisting for days following object removal⁴⁸, and inactivation of the LEC reduces rate-remapping in CA1 neurons and alters their responses to visual objects⁴⁹. The present findings indicate that CA1-projecting SUB neurons form a nexus point that is critical to object-place memory formation. These neurons are anatomically interconnected with several brain regions that are strongly implicated in encoding of object-location relationships, and can modulate spatially specific activity patterns of CA1 neurons in a manner that incorporates object-place information into episodic memories formed by cortico-hippocampal circuits.

The circuitry associated with CA1-projecting SUB neurons and its role in object-location learning and place-specific activity of CA1 neurons bears some analogy to the influence of the prefrontal cortex (via the thalamic nucleus reuniens) on the trajectory-specific modulation of CA1 place-specific activity⁵⁰. Together, these findings highlight the need to consider the potential that multiple top-down cortical circuits influence CA1 output through intermediaries, including the SUB and the nucleus reuniens. Such cortico-hippocampal circuits can be considered key avenues by which sensory input and planned action are bidirectionally integrated with cognitive maps in the hippocampus and the EC to yield intelligent behavior.

Online content

Any methods, additional references, Nature Research reporting summaries, source data, statements of code and data availability and associated accession codes are available at https://doi.org/10.1038/s41593-019-0496-y.

Received: 19 August 2018; Accepted: 9 August 2019; Published online: 23 September 2019

References

- Henriksen, E. J. et al. Spatial representation along the proximodistal axis of CA1. Neuron 68, 127–137 (2010).
- Kjelstrup, K. B. et al. Finite scale of spatial representation in the hippocampus. Science 321, 140–143 (2008).
- Xu, X., Sun, Y., Holmes, T. C. & Lopez, A. J. Noncanonical connections between the subiculum and hippocampal CA1. J. Comp. Neurol. https://doi. org/10.1002/cne.24024 (2016).
- Sun, Y. et al. Cell-type-specific circuit connectivity of hippocampal CA1 revealed through Cre-dependent rabies tracing. Cell Rep. 7, 269–280 (2014).
- Sun, Y., Nitz, D. A., Holmes, T. C. & Xu, X. Opposing and complementary topographic connectivity gradients revealed by quantitative analysis of canonical and noncanonical hippocampal CA1 inputs. eNeuro https://doi. org/10.1523/ENEURO.0322-17.2018 (2018).
- Witter, M. P. Connections of the subiculum of the rat: topography in relation to columnar and laminar organization. *Behav. Brain Res.* 174, 251–264 (2006).
- Cembrowski, M. S. et al. Dissociable structural and functional hippocampal outputs via distinct subiculum cell classes. *Cell* https://doi.org/10.1016/j. cell 2018 03 031 (2018)
- Naber, P. A., Witter, M. P. & Lopes Silva, F. H. Networks of the hippocampal memory system of the rat. the pivotal role of the subiculum. *Ann. NY Acad.* Sci. 911, 392–403 (2000).
- Morris, R. G., Schenk, F., Tweedie, F. & Jarrard, L. E. Ibotenate lesions of hippocampus and/or subiculum: dissociating components of allocentric spatial learning. *Eur. J. Neurosci.* 2, 1016–1028 (1990).
- Jackson, J. et al. Reversal of theta rhythm flow through intact hippocampal circuits. Nat. Neurosci. 17, 1362–1370 (2014).
- Berger, T. W., Swanson, G. W., Milner, T. A., Lynch, G. S. & Thompson, R. F. Reciprocal anatomical connections between hippocampus and subiculum in the rabbit evidence for subicular innervation of regio superior. *Brain Res.* 183, 265–276 (1980).

- Shao, L. R. & Dudek, F. E. Electrophysiological evidence using focal flash photolysis of caged glutamate that CA1 pyramidal cells receive excitatory synaptic input from the subiculum. J. Neurophysiol. 93, 3007–3011 (2005).
- Schwarz, L. A. et al. Viral-genetic tracing of the input-output organization of a central noradrenaline circuit. Nature 524, 88-92 (2015).
- Lo, L. & Anderson, D. J. A Cre-dependent, anterograde transsynaptic viral tracer for mapping output pathways of genetically marked neurons. *Neuron* 72, 938–950 (2011).
- Heimer-McGinn, V. R., Poeta, D. L., Aghi, K., Udawatta, M. & Burwell, R. D. Disconnection of the perirhinal and postrhinal cortices impairs recognition of objects in context but not contextual fear conditioning. *J. Neurosci.* 37, 4819–4829 (2017).
- Petreanu, L., Mao, T., Sternson, S. M. & Svoboda, K. The subcellular organization of neocortical excitatory connections. *Nature* 457, 1142–1145 (2009).
- Tsien, J. Z. et al. Subregion- and cell type-restricted gene knockout in mouse brain. Cell 87, 1317–1326 (1996).
- 18. Klausberger, T. & Somogyi, P. Neuronal diversity and temporal dynamics: the unity of hippocampal circuit operations. *Science* **321**, 53–57 (2008).
- Roy, D. S. et al. Distinct neural circuits for the formation and retrieval of episodic memories. Cell 170, 1000–1012.e1019 (2017).
- 20. Roth, B. L. DREADDs for neuroscientists. Neuron 89, 683-694 (2016).
- Kesner, R. P., Farnsworth, G. & Kametani, H. Role of parietal cortex and hippocampus in representing spatial information. *Cereb. Cortex* 1, 367–373 (1991).
- Cai, D. J. et al. A shared neural ensemble links distinct contextual memories encoded close in time. *Nature* 534, 115–118 (2016).
- 23. Ziv, Y. et al. Long-term dynamics of CA1 hippocampal place codes. *Nat. Neurosci.* 16, 264–266 (2013).
- Skaggs, W. E., McNaughton, B. L., Wilson, M. A. & Barnes, C. A. Theta phase precession in hippocampal neuronal populations and the compression of temporal sequences. *Hippocampus* 6, 149–172 (1996).
- Kanter, B. R. et al. A novel mechanism for the grid-to-place cell transformation revealed by transgenic depolarization of medial entorhinal cortex layer II. Neuron 93, 1480–1492.e1486 (2017).
- Miao, C. et al. Hippocampal remapping after partial inactivation of the medial entorhinal cortex. Neuron 88, 590–603 (2015).
- 27. Leutgeb, S. et al. Independent codes for spatial and episodic memory in hippocampal neuronal ensembles. *Science* **309**, 619–623 (2005).
- Crowley, P. H. Resampling methods for computation-intensive data-analysis in ecology and evolution. *Annu. Rev. Ecol. Syst.* 23, 405–447 (1992).
- Deshmukh, S. S. & Knierim, J. J. Influence of local objects on hippocampal representations: landmark vectors and memory. *Hippocampus* 23, 253–267 (2013).
- 30. Ji, D. & Wilson, M. A. Coordinated memory replay in the visual cortex and hippocampus during sleep. *Nat. Neurosci.* **10**, 100–107 (2007).
- Alexander, A. S. & Nitz, D. A. Retrosplenial cortex maps the conjunction of internal and external spaces. *Nat. Neurosci.* 18, 1143–1151 (2015).
- 32. Jacob, P. Y. et al. An independent, landmark-dominated head-direction signal in dysgranular retrosplenial cortex. *Nat. Neurosci.* **20**, 173–175 (2017).
- Czajkowski, R. et al. Encoding and storage of spatial information in the retrosplenial cortex. Proc. Natl Acad. Sci. USA 111, 8661–8666 (2014).
- Makino, H. & Komiyama, T. Learning enhances the relative impact of top-down processing in the visual cortex. *Nat. Neurosci.* 18, 1116–1122 (2015).
- Klausberger, T. GABAergic interneurons targeting dendrites of pyramidal cells in the CA1 area of the hippocampus. Eur. J. Neurosci. 30, 947–957 (2009).
- Agster, K. L. & Burwell, R. D. Hippocampal and subicular efferents and afferents of the perirhinal, postrhinal, and entorhinal cortices of the rat. Behav. Brain Res. 254, 50–64 (2013).
- 37. Hoydal, O. A., Skytoen, E. R., Andersson, S. O., Moser, M. B. & Moser, E. I. Object-vector coding in the medial entorhinal cortex. *Nature* **568**, 400–404 (2019).
- 38. Wang, C. et al. Egocentric coding of external items in the lateral entorhinal cortex. *Science* **362**, 945–949 (2018).
- Klausberger, T. et al. Brain-state- and cell-type-specific firing of hippocampal interneurons in vivo. Nature 421, 844–848 (2003).
- Maccaferri, G. & McBain, C. J. Long-term potentiation in distinct subtypes of hippocampal nonpyramidal neurons. *J. Neurosci.* 16, 5334–5343 (1996).

- 41. Barker, G. R. & Warburton, E. C. When is the hippocampus involved in recognition memory? *J. Neurosci.* **31**, 10721–10731 (2011).
- Deshmukh, S. S., Johnson, J. L. & Knierim, J. J. Perirhinal cortex represents nonspatial, but not spatial, information in rats foraging in the presence of objects: comparison with lateral entorhinal cortex. *Hippocampus* 22, 2045–2058 (2012).
- 43. Barker, G. R. et al. Separate elements of episodic memory subserved by distinct hippocampal-prefrontal connections. *Nat. Neurosci.* **20**, 242–250 (2017).
- Bussey, T. J., Duck, J., Muir, J. L. & Aggleton, J. P. Distinct patterns of behavioural impairments resulting from fornix transection or neurotoxic lesions of the perirhinal and postrhinal cortices in the rat. *Behav. Brain Res.* 111, 187–202 (2000).
- Taylor, K. I., Moss, H. E., Stamatakis, E. A. & Tyler, L. K. Binding crossmodal object features in perirhinal cortex. *Proc. Natl Acad. Sci. USA* 103, 8239–8244 (2006).
- Liu, P. & Bilkey, D. K. The effect of excitotoxic lesions centered on the hippocampus or perirhinal cortex in object recognition and spatial memory tasks. *Behav. Neurosci.* 115, 94–111 (2001).
- Ho, J. W. et al. Bidirectional modulation of recognition memory. J. Neurosci. 35, 13323–13335 (2015).
- Tsao, A., Moser, M. B. & Moser, E. I. Traces of experience in the lateral entorhinal cortex. Curr. Biol. 23, 399–405 (2013).
- Scaplen, K. M., Ramesh, R. N., Nadvar, N., Ahmed, O. J. & Burwell, R. D. Inactivation of the lateral entorhinal area increases the influence of visual cues on hippocampal place cell activity. Front. Syst. Neurosci. 11, 40 (2017).
- Ito, H. T., Zhang, S. J., Witter, M. P., Moser, E. I. & Moser, M. B. A prefrontal-thalamo-hippocampal circuit for goal-directed spatial navigation. *Nature* 522, 50–55 (2015).

Acknowledgements

This work was supported by NIH grants, including a BRAIN Initiative grant (NS104897 to X.X. and D.A.N), other grants (NS078434 to X.X.; MH105427 to X.X. and P.G.; U54 HD87101, NSF NeuroNex Hub 1700408 to P.G. and NS095355 to Q.N.), a NSF grant (DMS1763272 to Q.N.) and a Simons Foundation grant (594598 to Q.N.). T.C.H. is supported by grant R35 GM127102. P.Z. is supported by a NIH grant (NIBIB R01EB022913), a NSF NeuroNex award (DBI-1707398) and the Gatsby Foundation. The H129 virus was provided by L. Equist with the support of the Center for Neuroanatomy with Neurotropic Viruses (NIH grant P400D010996). This work was also made possible, in part, through access to the confocal facility of the Optical Biology Shared Resource of the Cancer Center Support Grant (CA-62203) at the University of California, Irvine.

Author contributions

X.X., Y.S. and D.A.N. designed the experiments. Y.S. and X.L. performed the viral tracing, miniscope imaging and mouse behavioral experiments. X.Q. and L.J. performed the electrophysiological recordings. S.J., K.G.J. and Q.N. performed the computational analyses. S.J., Y.S. and L.C. developed codes and analyzed imaging data with the help from P.Z., D.A.N. and Q.N. P.G. contributed to the miniscope imaging application. X.X., D.A.N., Y.S., T.C.H. and S.J. analyzed and interpreted the data, wrote the manuscript and prepared the figures. X.X. oversaw the project.

Competing interests

The authors declare no competing interests.

Additional information

 $\label{lem:supplementary} \textbf{Supplementary information} \ is available for this paper at \ https://doi.org/10.1038/s41593-019-0496-y.$

Correspondence and requests for materials should be addressed to D.A.N. or X.X.

Peer review information *Nature Neuroscience* thanks Aman Saleem, Sylvain Williams, and the other, anonymous, reviewer(s) for their contribution to the peer review of this work.

Reprints and permissions information is available at www.nature.com/reprints.

Publisher's note Springer Nature remains neutral with regard to jurisdictional claims in published maps and institutional affiliations.

© The Author(s), under exclusive licence to Springer Nature America, Inc. 2019

Methods

Animals. All experiments were conducted according to the National Institutes of Health guidelines for animal care and use, and were approved by the Institutional Animal Care and Use Committee and the Institutional Biosafety Committee of the University of California, Irvine. Please see Supplementary Table 4 for details of the animal strains, viral injections and experiments performed. No statistical methods were used to predetermine sample sizes, but our sample sizes were similar to those reported in previous publications^{4,5,51–53}. The data collection was randomized with respect to experimental conditions and groups whenever possible. Experimenters were not blinded to the experimental conditions during data acquisition, but imaging data and behavioral data analyses were performed blinded to treatment groups.

No animals or data points were excluded from the analyses unless specified in the Nature Research Reporting Summary.

Viral injections. The general procedure has been previously described^{4,5,54}. Mice were anesthetized with continuous 1% isoflurane and placed in a rodent stereotax (Leica Angle Two for mouse) and the head secured. A three-axis micromanipulator guided by a digital atlas was used to determine coordinates for the bregma and lambda. The following injection coordinates targeting the CA1 intermediate subfield were used: anteroposterior (AP): -1.94 mm; lateromedial (ML): -1.40 mm; and dorsoventral (DV): -1.35 mm (all values are given relative to the bregma). The following coordinates targeting the SUB were used: AP: -3.40; ML: -1.88; and DV: -1.70. A small drill hole was made in the skull above the injection site, exposing the pia surface. A glass pipette (tip diameter, $\sim\!20\text{--}30\,\mu\text{m}$) was loaded with virus and then lowered into the brain at the appropriate coordinates. A Picospritzer (General Valve) was used to pulse virus into the brain at a rate of 20-30 nl min⁻¹ with 10-ms pulse durations. To prevent backflow of virus, the pipette remained in the brain for 5 min after completion of the injection. Once the injection pipette was withdrawn, the mouse was removed from the stereotax, and the incision was closed with tissue adhesive (3M Vetbond). Mice were returned to their home cages to recover.

To target larger populations of excitatory neurons in the CA1 or SUB for rabies virus tracing, we crossed the LSL-R26^{Tva-lacZ} mouse line⁵⁵ with the Camk2a-Cre (T29) mouse line¹⁷. We term the double-transgenic mice as Camk2a-Cre;TVA mice, in which Cre-expressing cells also express TVA to restrict initial infection of EnvA-SADAG rabies virus. Mice (8-12 weeks old) of either sex were used for experiments and had free access to food and water in their home cages before and after surgeries. Genetically modified rabies viruses used for the experiments are deletion-mutant rabies viruses and are based on a vaccine strain (SADB19). The rabies viruses were made at the University of California, Irvine, with required cell lines and seeding viruses from E. Callaway's group at the Salk Institute for Biological Studies. For monosynaptic rabies virus tracing from the CA1 or subicular excitatory neurons, a total of 0.1 µl of the helper virus (AAV8-EF1a-FLEX-HB, 2×1011 genome units per ml, where H represents histone EGFP and B represents B19 rabies glycoprotein; Addgene, plasmid 37452) was injected into the CA1 or the SUB of Camk2a-Cre; TVA mice. Three weeks after the AAV injection, which allowed for the infected neurons to express high contents of rabies glycoproteins (RGs) and EGFP, the pseudotyped, RG-deleted rabies virus (EnvA-SAD Δ G-dsRed rabies, 0.2 µl, 2 × 10 9 infectious units per ml) was injected into the same location as the initial injection. The rabies virus was allowed to replicate and retrogradely spread from targeted Cre+ cell types to directly connected presynaptic cells for 9 days before the animals were perfused for tissue processing.

To map circuit input connections of CA1-projecting subicular neurons, $0.3\,\mu$ l of CAV2-Cre virus (3 × 10¹² infectious units per ml; purchased from E. J. Kremer's group, France) was delivered into the CA1 region of wild-type C57BL/6 mice to target CA1-projecting subicular neurons. CAV2-Cre is able to retrogradely transport into the SUB and express Cre selectively in CA1-projecting subicular neurons. Then, 0.1 μ l of AAV8-EF1a-FLEX-HTB (2 × 10¹¹ genome units per ml, where T represents TVA) was delivered into the SUB during the same surgery session. After 3 weeks, 0.2 μ l of EnvA-SAD Δ G-mCherry rabies virus was injected into the same SUB location. For control experiments to verify the retrograde efficiency and to test the viral tropism of CAV2-Cre, we injected the CAV2-Cre virus (0.4 μ l) into the CA1 of the Ai9 tdTomato reporter line 56 . The Ai9 animals were perfused for tissue processing 3 weeks after injection.

To map output projections of CA1-projecting subicular neurons, CAV2-Cre virus was first delivered into the CA1 region. Two weeks after the CAV2-Cre injection, 0.4 μl of Cre-dependent anterograde-directed HSV (H129 Δ TK-TT 14 , provided by L. Enquist at Princeton University) was injected into the SUB. The H129 virus was allowed to replicate and anterogradely spread from targeted Cre+cell types to directly connected postsynaptic cells within 48 h before the animals were perfused for tissue processing.

For genetic inactivation of CAI-projecting subicular neurons using DREADD, 0.3 μ I of the CAV2-Cre virus was bilaterally delivered into the intermediate CA1 region (AP: $-1.94\,\mathrm{mm}$; ML: $\pm1.40\,\mathrm{mm}$; DV: $-1.35\,\mathrm{mm}$) in wild-type C57BL/6J mice, followed by bilateral injection of 0.3 μ I of AAV2-DIO-hM4D-mCherry (3.7 \times 10 12 genome units per ml; UNC Vector Core) in the SUB (AP: $-3.40\,\mathrm{mm}$; ML: $\pm1.96\,\mathrm{mm}$; DV: $-1.67\,\mathrm{mm}$) in the same surgery session. Mice were then allowed to recover in their home cages for 3 weeks before behavior experiments.

For genetic activation of CA1-projecting subicular neurons, $0.2\,\mu l$ of rAAV2-retro-hSyn-Cre virus⁵⁷ (packaged by ViGene Biosciences, 1.9×10^{13} genome copies per ml) was bilaterally delivered into the intermediate CA1 region of Ai32 mice⁵⁸ expressing an improved Chr2-ehanced yellow fluorescent protein (EYFP) fusion protein following exposure to Cre recombinase. Application of rAAV2-retro in the CA1 injection site can retrogradely transport into the SUB and express Cre to activate ChR2 expression specifically in CA1-projecting subicular neurons. Our histological examination indicated that, in contrast to CAV2-Cre, rAAV2-retro-hSyn-Cre does not infect local cell bodies in the CA1, which prevents ChR2 expression in the axons of CA1 neurons. For control experiments with EGFP expression, rAAV2-retro-hSyn-EGFP virus was used instead.

To image in vivo calcium transients of CA1 neurons with inactivation of CA1-projecting subicular neurons on the linear track, the following injections were performed: 0.2μ l of AAV1-CaMKII-GCaMP6f-WPRE-SV40 (Penn Vector Core; 3.7×10^{13} genome copies per ml) was injected into the CA1 (0.2 mm posterior and lateral to the injection site of the CAV2-Cre); $0.3\,\mu$ l of CAV2-Cre virus was delivered into the right intermediate CA1 region of C57BL/6 mice; and $0.3\,\mu$ l of AAV2-DIO-hM4D-mCherry was delivered into the ipsilateral side of the SUB during the same surgery session. We opted to use DREADD-mediated inactivation over optogenetic silencing for imaging experiments because of the convenience of systemic ligand delivery and the lack of light interference with miniature microscopic imaging. To image in vivo calcium transients of CA1 neurons with inactivation of CA1-projecting subicular neurons in the open-field and during OLM tasks, a similar viral injection strategy was used, but CAV2-Cre and AAV2-DIO-hM4D-mCherry was delivered bilaterally to match the OLM behavioral experiments.

Histology, immunochemical staining and viral tracing data analyses. The mice were transcardially perfused, and their brains were removed and left in 4% paraformaldehyde overnight. Samples were then transferred into 30% sucrose in PBS the next day. The brain was sectioned coronally into 30-µm-thick samples on a freezing microtome (Leica SM2010R). Every third section was mounted for examination and quantification of starter cells and their presynaptic cells in different brain structures. For mapping input connections to CA1-projecting subicular neurons, selected sections were stained with a GFP antibody to amplify the EGFP signal resulting from the helper AAV expression for the robust identification of starter cells. A chicken anti-GFP primary antibody (Aves Labs, 1:500 dilution) followed by an Alexa Fluor (AF) 488-conjugated donkey antichicken secondary antibody (Jackson ImmunoResearch, 1:200 dilution) was applied to the sections. To immunochemically identify neuronal cells, NeuN immunostaining was used with a mouse anti-NeuN primary antibody (Millipore, 1:100) followed by an AF488-conjugated donkey anti-mouse secondary antibody (Jackson ImmunoResearch, 1:200). To immunochemically identify GABAergic cells, GABA immunostaining was performed using a rabbit anti-GABA primary antibody (Sigma-Aldrich, 1:1,000) followed by an AF488- or AF647-conjugated donkey anti-rabbit secondary antibody (Jackson ImmunoResearch, 1:200 dilution). For the H129 virus tracing experiments, we performed immunostaining to amplify tdTomato signals with a rabbit anti-dsRed antibody (Clontech, 1:250 dilution) followed by a Cy3-conjugated donkey anti-rabbit secondary antibody (Jackson ImmunoResearch, 1:200 dilution). For CaMKII immunostaining, a rabbit polyclonal antibody (Santa Cruz Biotechnology, 1:500 dilution) was used followed by an AF488-conjugated donkey anti-rabbit secondary antibody. For somatostatin immunostaining, a rat monoclonal primary antibody (EMD Millipore, 1:200 dilution) was used and followed by an AF488-conjugated donkey anti-rat secondary antibody. Sections were counter-stained with 10 µM 4,6-diamidino-2phenylindole (DAPI), then mounted and cover-slipped. Please see our previous 9-61 and the Nature Research Reporting Summary for detailed information regarding the relevant antibody characterization and specificity in these and other immunostaining experiments.

Brain slice images were acquired using an automated slide scanning and analysis software (Metamorph) in a high-capacity computer coupled with a fluorescence BX61 Olympus microscope and a high-sensitivity Hamamatsu CCD camera. In addition, we imaged labeled cells in selected sections with a confocal microscope (LSM 700/780, Carl Zeiss) coupled with z-stack and tile-scanning features under a 20× objective lens. Quantitative examinations across the series of sections were conducted for complete and unbiased analyses of virally labeled neurons by using either Metamorph or Adobe Photoshop software (Adobe Systems).

Slice electrophysiology. To complement virus-based circuit mapping, we used our established functional-mapping approach to perform CRACM using a previously described protocol 16 . First, AAV1-CAG-ChR2-Venus was injected into the dorsal SUB iontophoretically by using a Digital Midgard Precision Current Source (Stoelting). The virus was delivered by applying currents of positive $3\,\mu\text{A}$ in an alternative mode with a cycle of 7s on and 7s off for 5 min. After recovery, mice were housed in the animal facility for 3 weeks before slice experiments.

Coronal sections of $400\,\mu m$ were cut from the dorsal hippocampus with a vibratome (VT1200S, Leica Biosystems) in sucrose containing artificial cerebrospinal fluid (ACSF), which contains the following (in mM): 85 NaCl,

75 sucrose, 2.5 KCl, 25 glucose, 1.25 NaH $_2$ PO $_4$, 4 MgCl $_2$, 0.5 CaCl $_2$ and 24 NaHCO $_3$. Slices were incubated for at least 30 min in normal ACSF (in mM: 126 NaCl, 2.5 KCl, 26 NaHCO $_3$, 2 CaCl $_2$, 2 MgCl $_2$, 1.25 NaH $_2$ PO $_4$ and 10 glucose) at 32 °C before transfer into slice-recording chambers. Throughout the cutting, incubation and recording, the solutions were continuously supplied with 95% O $_3$, and 5% CO $_3$.

Whole-cell recordings were performed under a differential interference contrast/fluorescence microscope (BX51WI, Olympus). To target whole-cell recordings, cells were visualized at high magnification ($60\times$ objective, 0.9 numerical aperture; LUMPlanFl/IR, Olympus). Cell bodies of recorded neurons were at least 50 μ m below the surface of the slice. Patch pipettes ($4-6\,{\rm M}\Omega$ resistance) made of borosilicate glass were filled with an internal solution containing the following (in mM): 126 K-gluconate, 4 KCl, 10 HEPES buffer, 4 ATP-Mg, 0.3 GTP-sodium and 10 phosphocreatine (pH7.2, 300 mOsm). Electrodes also contained 0.1% biocytin for post hoc cell labeling and further morphological identification. Once stable whole-cell recordings were achieved with good access resistance (usually <30 M Ω), basic electrophysiological properties were examined through hyperpolarizing and depolarizing current injections.

During CRACM experiments, TTX (1 µM) and 4-AP (100 µM) were added to the bath solution to block Na+ channels and the K+ channels that are critical for repolarization of the axon so that spatially restricted activation of ChR2expressing subicular axons with a 473-nm blue laser (~3 mW/5.5 mm², 0.25 ms; laser spot diameter, ${\sim}50\,\mu\text{m})$ only occurred in the vicinity of the laser beam (with action potentials blocked), enabling functional assessments of direct and monosynaptic synaptic connectivity. We used sequential stimulation of the blue laser at 16×16 different sites arranged in a mapping grid covering most of the hippocampal slice in a nonraster, nonrandom sequence to avoid revisiting the vicinity of recently stimulated sites. Simultaneous whole-cell voltage-clamp recordings were made from CA1 pyramidal neurons to measure optogenetic stimulation-evoked excitatory postsynaptic current (EPSC) responses at the holding potential around -70 mV. The EPSC response from each stimulation site was the measurement of the sum of total EPSCs within the analysis window (10 ms to 160 ms post photostimulation), with the baseline spontaneous response subtracted from the photostimulation response of the same site. The value was normalized against the duration of the analysis window (that is, 150 ms) and expressed as the average integrated amplitudes in picoamperes (pA). For the colorcoded map display, data were plotted as the average integrated EPSC amplitude per pixel location (stimulation site), with the color scale coding for input strength. After physiological assays had been completed, brain slices were fixed in 4% paraformaldehyde in PBS overnight and transferred to 30% sucrose solution in PBS. The slices were stained against biocytin with 1:1,000 Cy3-conjugated streptavidin (Jackson ImmunoResearch) to show the morphology of the recorded cells. Neuron reconstructions were computer-assisted and based on stacks of optical sections acquired by a confocal microscope (LSM 700/780, Carl Zeiss).

We also provided direct evidence from in vitro recordings of SUB neurons bearing DREADD to show that CNO potently inhibits these neurons. *Camk2a*-Cre mice were injected with AAV2-DIO-hM4D-mCherry injection in the SUB. Three weeks following viral injection (time-matched with the behavioral experimental time point), slice electrophysiology experiments were conducted. The hM4D-expressing neurons were targeted based on their mCherry fluorescence. We also recorded from a few non-mCherry-expressing neurons for control experiments. To examine hM4D/CNO-mediated inactivation, 5 µM CNO in the recording solution was applied. The ligand application for 20 min was estimated to produce full hM4D/CNO effects, while the washout of 30–45 min was used to remove the CNO to assess post-control responses. Given hM4D is a G protein-coupled receptor, CNO effects can only be partially reversed with this washout, which is consistent with published results⁶²⁻⁶⁴. We focused on analyzing neuronal resting membrane potentials, spiking thresholds, and spike numbers at different steps of depolarizing current pulses at baseline, in the presence of CNO, and after its washout.

In addition, we performed in vitro electrophysiological recording of SUB neurons in response to blue laser stimulation in brain slices. *Camk2a*-Cre mice were injected with AAV1-DIO-ChR2-YFP injection in SUB. Three weeks following viral injection, slice electrophysiology experiments were conducted. ChR2-expressing SUB neurons were recorded, and examined with the ChR2 stimulation protocol (6 Hz, 50 ms for 3–15 min) applying a matched light intensity of in vivo behavioral experiments. ChR2-expressing neurons were modulated by blue laser stimulation and remained healthy. About half of the 15 recorded cells could faithfully spike following laser stimulation, while the other half of cells responded less reliably with spikes (but with clear modulation of subthreshold membrane potentials).

Mouse behavior experiments of OLM, novel object recognition and the dryland version of the Morris water maze task. Before experiments, all mice were handled for 2 min per day for 6 days and were habituated to the experimental apparatus for 6 min per day for 3 consecutive days without objects. The experimental chamber was a rectangular open-field arena with fixed local and distal cues $(20\,\mathrm{cm}\times40\,\mathrm{cm}\times20\,\mathrm{cm})$, manufactured by a local workshop at the University of California, Irvine). There were two identical objects presented to the animal in the box during the training phase of the OLM and novel object recognition experiments. Animals were allowed to freely explore the box and the

objects for 10 min. During a 5-min test at 24 h after the training, animals were allowed to freely explore the box with one of the objects from training having been moved to a new location. For the novel object recognition experiments, animals were allowed to freely explore the box with one of the objects from training replaced with another object with distinct geometry and appearance. Two different objects were used in a counterbalanced manner during the object recognition experiments.

For the behavioral experiments with in vivo optogenetic stimulation, fiber optic ferrules were bilaterally implanted targeting the dorsal SUB at 2 weeks after the virus injection. During the habituation and behavioral testing sessions for all mice, one end of the bifurcated optic fiber was connected to a rotary joint (Doric Lenses) on the ceiling of the behavioral box, the other end was connected to the bilateral implants. Laser delivery was at 6 Hz, 50 ms duration using a 450-nm laser during the entire 3-min training session for the optogenetic stimulation group and the control group with the EGFP control vector injected. The laser was off for the no-laser control group during training. Our decision to use theta-frequency patterned stimulation was based on prior work showing that theta-patterned stimulation in the septal nucleus could improve performance on spatial tasks and that stronger theta-frequency signaling in the hippocampus is correlated with stronger spatial performance^{65,66}. It is also the case that both the hippocampus and the SUB share strong co-modulation (coherence) of spatial firing according to theta-frequency oscillations¹⁰. For these reasons, we felt that theta-paced as opposed to randomly paced stimulation might be better with respect to not disrupting theta rhythms. There was no laser delivered for all groups during the 5-min retention test. The laser power at the implant fiber tip was 2-3 mW/5.5 mm² at a steady state, and it was measured 0.7-0.9 mW/5.5 mm² with the delivery at 6 Hz, 50 ms duration. For behavioral experiments with DREADD inactivation, mice were intraperitoneally injected with CNO (1.4 mg per kg) or saline 45 min before training. As the optimal use of CNO as a DREADD ligand has been a topic of important discussion 67,68, we examined the parameters that reflect the behavioral states of the animals, such as maximum running speeds and the number of running laps across control, CNO and post-control sessions, and did not find any significant differences (Supplementary Fig. 7d-f). Furthermore, the administration of CNO at our dosage to control mice that expressed no DREADD did not influence their OLM performance69.

Video recordings of the experiments were made using the software ANY-MAZE (Stoelting) and analyzed offline using customized software to score the retention times to each object with standardized criteria as previously described 51,70,71 . The interaction/exploration time of a mouse with the object is defined as the mouse's nose being within 1 cm of the object and pointing directly at the object so that an elongated line from its eyes to nose would hit the object. However, the following behaviors were excluded from the exploration time: (1) times for which the mouse did not approach the object (for example, if the mouse re-orientates itself and the nose accidentally comes close to the object); (2) the mouse mounted the top of the object (even if it is looking down at the object); (3) the mouse reared on the object but is looking over the object (for example, looking at the ceiling); (4) the mouse engaged in a repetitive behavior (such as digging close to the object or bitting the object). The DI was defined as follows: $(T_{\rm moved} - T_{\rm unmoved})/(T_{\rm moved} + T_{\rm unmiliar}) \times 100\%$.

To enhance the characterization of the behavioral function of the SUB-CA1 projection, we implemented a dry-land version of the often-used Morris water maze test (an adaptation of a previously described method21) to test how DREADD-based inactivation of CA1-projecting SUB neurons affects performance on a spatial navigation task (Supplementary Fig. 5). In the dry-land task, similar to the Morris water maze task, solving the task demands localization of a target in the frame of reference defined by distal visual cues (commonly known as allocentric space). It does not demand knowledge of the location of proximal cues, and the possible use of proximal cues is avoided by careful attention to clearing the maze surface of odors between trials and by rotating the surface relative to the environment. Thus, this behavioral task allows for a comparison of performance on the object-location task with that on a more purely spatial task related to localization in allocentric space. As illustrated in Supplementary Fig. 5c, the maze comprises a round board with a diameter of 60 cm and 37 wells each holding an interchangeable plastic cup (3 cm in diameter each). The wells are uniformly spread across it in a squared grid pattern. Following handling, water-deprived mice were allowed to explore on the board and drink water from the cups for 10 min of habituation for 2 days; all cups in the board except the 16 most peripheral ones were filled with 20 µl of water each. During the first phase of pre-training (days 1-2), only one of the cups in a semi-randomly chosen quadrant of the arena had 60 µl water and it was flagged with a silver metal post close to the well (Supplementary Fig. 5c, left). The animal was released facing the edge of the board from the three other quadrants with eight trials per day. The water cup location was changed to a new quadrant on each pre-training day. For each trial, the animal was allowed to explore, look for the target and drink water until a total of 2 min had passed. During the second phase of the pre-training period (days 3-4), the procedure was identical to the previous 2 days, except for the exploration time; we ended trials once the animal located and drank water from the target cup. On training day (day 5), the cohort of mice (10 mice) were either injected with CNO or saline (5 mice each) 45 min before trials began. The first four trials were run with

the flag marker set close to the target cup location, and the last four trials were run without the flag at the same location (Supplementary Fig. 5c, right). The water cup location differed from those used during pre-training, but remained in the same location for the subsequent testing (day 6). Animals ran eight trials with the target cup location unmarked on the testing day. Subsequently, animals remained in their home cages for 2 days, and then began a second pair of training and testing (days 9–10) using a new location with reversed CNO or saline treatment for different groups. A video camera was positioned directly above the round board, and all trials were videotaped and tracked.

Latency to finding the target cup location and distance traveled to find the location were measured. Tracking in the video images was performed using a custom-written Matlab script. First, the external boundary of the dry-land maze platform was segmented from the background, and the area inside the boundary was regarded as the region of interest (ROI) for trajectory detection. The ears and tail of a mouse were segmented based on their grayscale values. Two manually selected thresholds defined the grayscale intervals where the ears and tail could be distinguished from the remaining elements inside the ROI. The ears were further distinguished from the tail by their ratios of the major axis length and minor axis length of the segmented elements. The element with a ratio less than three was regarded as the ear, while the other region was regarded as the tail. The trajectory was tracked with the ear positions in the video. Given that the time when the mouse was released on the platform was time 1 and the time when the mouse reached the targeted water well was time 2, the latency time of reaching the target was defined as the difference between time 2 and time 1. The corresponding distance was defined as the total traveling distance of the mouse between time 1 and time 2.

Miniscope imaging preparation, GRIN lens implantation, baseplate placement and mouse linear track and open-field mapping. At 2 weeks after AAV1-CaMKII-GCaMP6f injection, a gradient refractive index (GRIN) lens was implanted at the injection site in the CA1. A 1.8-mm diameter circular craniotomy was centered at the following coordinates: AP: -2.30 mm and ML: +1.75 mm relative to bregma. ACSF was repeatedly applied to the exposed tissue, and the cortex directly below the craniotomy was aspirated with a 27-gauge blunt syringe needle attached to a vacuum pump. The unilateral cortical aspiration might affect part of the anteromedial visual area determined using the Allen Brain Atlas (www. brain-map.org/), but the procedure left the primary visual area intact. The GRIN lens (0.25 pitch, 0.55 numerical aperture, 1.8-mm diameter and 4.31 mm in length, Edmund Optics) was slowly lowered using a stereotaxic arm to the CA1 to a depth of -1.55 mm relative to the bregma. Next, a skull screw was used to anchor the GRIN lens to the skull. Both the GRIN lens and skull screw were fixed with cyanoacrylate and dental cement. Kwik-Sil (World Precision Instruments) was used to cover the lens. Two weeks later, a small aluminum baseplate was cemented onto the head of the animal atop the existing dental cement. A miniscope was fitted into the baseplate and locked in a position so that the field of view was in focus to visualize GCaMP6f-expressing neurons and visible landmarks, such as

To motivate animals to run on a linear track, access to water was regulated between every Sunday afternoon and every Friday afternoon. Mice were provided water starting at 1 ml per day and with adjustments up or down until weights stabilized around 82-85% of their original body weight. In the meantime, mice were handled 5 min per day for 3 days. As illustrated in Supplementary Fig. 7, mice were trained to run on a 1-meter linear track with water rewards placed at both ends of the track for 60 laps per session for 5 days. Mice were then trained with a head-mounted miniscope (without recording) to run on the linear track with water reward for 60 laps per session for another 5 days. After all training was completed, in vivo GCaMP6f-based calcium imaging of population CA1 neurons in awake behaving mice was performed for the linear track experiments with miniscope recordings for two sessions of baseline control, two sessions of CNO inactivation and two sessions of post-baseline control. To avoid GCaMP6f fluorescence bleaching, mice usually ran 1 session every other day, with 15-min recording. CNO was administered via intraperitoneal injection 45 min before imaging (saline was administered during control and post-control sessions in the same way). Intervals between the last CNO session and the first post-control session were longer than 48 h to ensure clearance of CNO.

For the open-field experiments, mice were handled for at least 1 week and habituated for intraperitoneal injections and head-mounted miniscopes. Mice were then habituated for 3 days in an open-field arena with miniscopes for 15 min each day. The open-field arena was a circular environment (36 cm in diameter) with fixed local and distal cues. Mice were randomly divided into two groups, with one group receiving CNO injection for DREADD-based inactivation of CA1-projecting SUB neurons. On day 1, mice from both groups explored in the open-field arena for 15 min each while calcium signals from CA1 neurons were recorded. These recordings acted as baseline controls. On day 2, mice from the saline control group received a single dose of saline injections 45 min before the open-field recording, while mice from the CNO-treated group received a single dose of CNO injections (1.4 mg per kg) 45 min before the open-field recording. Day 3 was off to ensure clearance of CNO. Experiments on day 4 were similar to day 1; mice from both groups explored in the open-field arena for 15 min each with miniscope imaging. These recordings were used as post-controls.

For miniscope imaging during OLM tasks, mice were habituated for 3 days in the OLM behavior box with miniscopes for $10\,\mathrm{min}$ each day. For baseline recordings, animals were put in the OLM behavior box without objects and released for $10\,\mathrm{min}$. At $45\,\mathrm{min}$ before training, mice were randomly divided into two groups, and one group received saline injections while the other group received CNO ($1.4\,\mathrm{mg}$ per kg) injections. During recordings in training, two identical objects were presented to the animal during the $10\,\mathrm{min}$ training session. For the retention test, one of the two objects were moved to a new location and the animals were allowed to explore for $10\,\mathrm{min}$ to attain sufficient coverage for calcium imaging analysis. With respect to behavior, we found that the $10\,\mathrm{min}$ retention test gave rise to a more robust measurement with less variability in the DI compared with the data analyzed based on the first $5\,\mathrm{min}$ of recording.

The linear track, open-field and OLM experiments were performed in a dedicated animal behavior testing room. Two distinct shelving racks (195-cm height × 122-cm width versus 178-cm height × 152-cm width) with different objects and visual cue decorations were placed against the north and east walls of the room. Two identical fear-conditioning boxes (60-cm tall) were placed against the west wall of the room. The linear track was placed in parallel to the north rack with distinct visual cues at each end of the track. The open-field enclosure was placed against the southwest edge of the east rack with cue cards inside to serve as local cues. The OLM testing arena was placed against the northwest edge of the east rack with 5-cm-wide cue tape on the east wall of the enclosure. All the environments and cues remained constant during the entire series of the experiments.

Miniscope imaging data acquisition and analyses. Please refer to a previous publication and www.miniscope.org/ for technical details of our custom-constructed miniscopes. The head-mounted scope has a mass of about 3 g and uses a single, flexible coaxial cable to carry power, control signals and imaging data to custom open-source data acquisition (DAQ) hardware and software. Under our experimental conditions, the miniscope has a 700 $\mu m \times 450 \, \mu m$ field of view with a resolution of 752 pixels \times 480 pixels ($\sim 11 \, \mu m$ per pixel). The electronics packaged the data to comply with the USB video class protocol and then transmitted the data over SuperSpeed USB to a PC running custom DAQ software. The DAQ software was written in C++ and uses Open Computer Vision libraries for image acquisition. Images were acquired at ~ 30 frames per s and recorded to uncompressed avi files. The DAQ software simultaneously records the behavior of an animal through a high-definition webcam (Logitech) at ~ 30 frames per s, with time stamping of both video streams for offline alignment.

Calcium imaging data processing. Miniscope videos of individual sessions (that is, control, CNO and post-control sessions) were first concatenated and downsampled by a factor of two using NIH ImageJ software, and then motion-corrected using the NoRMCorre MATLAB package72. Next, we visually inspected the maximum intensity projection images of individual video sessions and manually performed minor linear translations to align videos of CNO and post-control sessions to the control session videos. Then, we created a large combined dataset by concatenating all aligned video images of control, CNO and postcontrol sessions using NIH ImageJ. While this large data concatenation required significant computer resources (that is, 28 cores, 128 GB dynamic random-access memory, 1 TB solid state drive, 8 TB hard disk drive), it greatly enhanced our ability to obtain cross-session cell tracking from different days (Supplementary Fig. 7a), which made it unnecessary to perform individual map alignment or cell registration across sessions and facilitated hippocampal activity re-mapping experiments. Subsequent analysis was performed using custom Matlab scripts. We adopted the newly developed method of extended constrained non-negative matrix factorization for endoscopic data (CNMF-E)73 to extract the calcium activity of individual neurons. The CNMF-E is based on the CNMF framework⁷⁴, which enables simultaneously denoising, deconvolving and demixing of calcium imaging data. Its key features include modeling the large rapidly fluctuating background that has a low spatial-frequency structure and allows good separation of singleneuron signals from this background (see a previous publication⁷³ for details). After iteratively solving a constrained matrix factorization problem, CNMF-E extracts the spatial footprints of neurons and their associated temporal calcium activity. Specifically, the first step of estimating the temporal activity of a neuron (a scaled version of dF/F, which is a metric used in most calcium imaging literature) is computing the weighted average of fluorescence intensities after subtracting the temporal activity of other neurons within the region of interest of that neuron. Then, a deconvolution algorithm, OASIS75, was applied to obtain the denoised neuron activity and deconvolved spiking activity, as illustrated in Supplementary Fig. 6b. Using the behavioral tracking video data, the position and speed of the animal was determined using a custom Matlab script. We identified the time points at which the speed of the animal was lower than 3 cm s⁻¹ on the linear track and excluded them from further analysis. We then temporally aligned the position data to the calcium imaging data using linear interpolation.

Calculation of positional calcium event rates. Once the deconvolved spiking activity of the neurons was extracted, we localized effective neuronal calcium events using a threshold (that is, 10% to the maxima in linear track experiments) to deconvolved spiking activity across all the sessions. To characterize the neural activity, we

calculated individual the positional event rate of the neuron by dividing the total number of events of each neuron at each bin location by the total occupancy time at each location, where locations were defined by sorting the behavior tracking data into 2.7 cm × 2.7 cm bins after excluding 5% of the total length on either end of the linear track. Calcium event-rate maps were smoothed using a two-dimensional convolution with a Gaussian filter with a standard deviation of 2 cm. To find the infield peak event rates for a place cell, the unsmoothed event-rate maps were used, and bin locations with a total occupancy time of less than 0.2 s were excluded. To determine the place field shift of the same place cell longitudinally, we calculated two-dimensional cross-correlations of the smoothed event-rate maps across different days. The cross-correlogram between event-rate maps across two different sessions of matched neurons were computed and then the Euclidian distance of the bin with the highest correlation was determined from physical centers of the crosscorrelogram. This method⁷⁶ circumvents the difficulty of matching individual fields across days, which becomes inaccurate when multiple place fields are detected in at least one of the recording sessions.

Spatial information statistics. To quantify the spatial location specificity of calcium events in terms of the information content of cell activity, spatial information scores in bits s-1 and bits per event were calculated for each neuron according to the following formula²⁴:

owing formula²⁴: Information score (bits s^{-1}) = $\sum_{i=1}^{n} P_i \lambda_i \log_2 \frac{\lambda_i}{\lambda}$ Information score (bits per event) = $\sum_{i=1}^{n} P_i \frac{\lambda_i}{\lambda} \log_2 \frac{\lambda_i}{\lambda}$, where P_i is the probability of

the mouse occupying the *i*-th bin for the neuron, λ_i is the event rate of the neuron in the *i*-th bin, while λ is the mean rate of the neuron across the whole session. Bins with a total occupancy time of less than 0.2 s were excluded from the calculation. To define place cells, event locations for each neuron were shuffled 1,000 times and spatial information (bits s⁻¹) was recalculated for each shuffle. This generated a distribution of shuffled information scores for each individual neuron. The value at 95% of each shuffled distribution was selected as the threshold for designation of the corresponding individual place cell. Neurons with less than ten calcium events for a given session were excluded.

Classification of place cells. We categorized place cells into different groups according to their individual changes in cross-session spatial information scores (bits s⁻¹). For each place cell, we examined whether its spatial information score in the CNO session was significantly different from that in both the control and postcontrol sessions using a jackknife resampling technique28. To do so, each trackrunning session was divided into ten equal-duration sub-sessions. We then applied jackknife resampling to the full recording session, each time calculating bits svalues by omitting one subsession. Therefore, for each place cell, the extended set of bits s-1 values, produced by this jackknife resampling procedure, include ten values, which are denoted by x_i (i=1,...,10). The mean and variance of this sampling distribution were as follows:

$$\bar{x} = \frac{1}{10} \sum_{i=1}^{10} x_i, V_x = \frac{9}{10} \sum_{i=1}^{10} (x_i - \bar{x})^2$$

After calculating \bar{x} and V_x from the CNO session, we contrasted it against the output from another session, for example \bar{y} and V_y from the control session. Then, we constructed a jackknife-based t-test, where the statistical test value Q could be calculated as

$$Q = \frac{\bar{x} - \bar{y}}{\sqrt{V_x + V_y}}.$$

A P value was calculated for Q from a standard normal distribution, and a significance level of 0.05 was used to determine whether they are significantly different. Each place cell was assigned to an appropriate group if its spatial information score in the CNO session was significantly different from that in both the control and post-control sessions. A place cell was classified as 'bit decrease' only when its spatial information score in the CNO session was significantly lower than both the control and post-control sessions, and vice versa for the 'bit increase' classification. A place cell that passed the statistical test in the CNO versus control and versus post-control in the opposite directions was classified into the 'unrecovered' group. The remainder of the place cells, which failed at least one of the statistical tests, were unassigned and excluded from the category analysis.

Open-field data analysis. Most of the analysis conducted for open-field experiments was similar to that for the linear track experiments. Briefly, the time points at which the speed of the animal was lower than 2 cm s⁻¹ were excluded from further analysis. Once the temporal activity of the neurons was extracted, we localized neuronal calcium events using a threshold of three times the standard deviation of the calcium signals across all the sessions. To characterize the neural activity, we calculated the positional event rate of individual neurons by dividing the total number of events of each neuron at each bin location by the total occupancy time at each location (each 2 cm × 2 cm bin of behavior tracking data). In calculating the spatial information scores of neural activity, bins with occupancy times of less than 0.2 s were excluded.

Miniscope imaging data analysis of OLM tasks. We constructed calcium event-rate maps in the same manner as the linear track experiment by sorting the behavior tracking data into bins of 1.5 cm × 1.5 cm. The bins with a total occupancy of less than 0.1 s were regarded as unvisited and were not included in the rate map. For each mouse, the ensemble event rates are the summation of events from all neurons normalized by the time spent at each location. Of note, the individual neuron's event rate associated with the object was quantified as the average event rate across bins within 3 cm surrounding the object. The total sum of an individual neuron's event rates of all CA1 neurons was defined as the ensemble event rate associated with the object. The relative event rate (ER) was expressed as a neural DI as follows: $(ER_{moved} - ER_{unmoved})/(ER_{moved} + ER_{unmoved}) \times 100\%$. Here, ER_{moved} and ER unmoved are the ensemble event rates associated with the moved and unmoved objects, respectively.

Place cell fields were determined using the approach described in a previous study77, and were located by finding the centers of calcium activity from the binned event-rate maps. The fields too close to each other (defined as less than 70% of the half distance between the center point of the spatial autocorrelation map and the closest local maximum) were removed. Place fields with in-field event rates that did not reach 25% of the peak event rate of the rate map were also excluded. We measured individual place fields whose peaks were located within a 3-cm radius of either object.

Position decoding using a neural network model. We built a neural network model to predict the position of mice during track running given the temporal activity of a specific set of CA1 neurons. Feedforward neural networks involve sequences of nonlinear transforms and are composed of linear transformations (weights) of input data, forming layers of hidden units. Using the Tensorflow library, we created a fully connected feedforward neural network with three hidden layers, with rectified linear unit activations after each hidden layer as the nonlinearities. We included dropout (at 50%), L, regularization and batch normalization to regularize the model^{78,79} and to decrease generalization error. The network was trained using the ADAM optimizer80. Ten percent of the linear track from both ends was removed, and the neural data were normalized using zscores. As input to the neural network, we took 10-20 timesteps of neural activity data from each side of the temporal point at which we wished to predict position. The hyperparameters (that is, the number of neurons per layer and the amount of neural data as input) of the model were determined by fivefold cross-validation. We split the data from the first control session into a training set (80% of data) and a contiguous testing set (20% of data). After training, the model was used to predict position on the testing set. We applied the trained model based on the first control session to the other sessions (for example, CNO and post-control) to investigate the effects of subicular inactivation on position decoding. Prediction (decoding) error was then computed as the mean absolute difference between the predicted and actual position on the horizontal track, which was formulated as $\sum_{t=1}^{\infty} |y_t - \hat{y}_t|/N$ where y_t represents the actual position of the animal at the t-th timestep, \hat{y}_t is the position decoded by our model and N is the number of data points in the test set for any given session (that is, 20% of the control data and 100% of the CNO and post-control data).

Statistical analyses. Data are presented as the mean \pm s.e.m, the mean \pm s.d. or the median ± interquartile range (IQR), as indicated. For statistical comparisons between groups, the data were checked for normality of distribution. If the criteria were met, a t-test was performed to compare two groups, otherwise, a Mann-Whitney U-test was used. For statistical comparisons across more than two groups, one-way analysis of variance (ANOVA) and related multiple comparison tests were used for group comparisons. For paired statistical comparisons, a paired t-test was used. For data with repeated measurements for more than two groups, repeated measures ANOVA and related multiple comparison tests were used to compare groups. In all experiments, the level of statistical significance was defined as $P \le 0.05$.

Reporting Summary. Further information on research design is available in the Nature Research Reporting Summary linked to this article.

Data availability

The datasets generated for the current study are available from the corresponding authors upon reasonable request.

Code availability

The custom code used for the analyses for the current study is available from the corresponding authors upon reasonable request.

References

- 51. Haettig, J., Sun, Y., Wood, M. A. & Xu, X. Cell-type specific inactivation of hippocampal CA1 disrupts location-dependent object recognition in the mouse. Learn. Mem. 20, 139-146 (2013).
- 52. Sun, Y. et al. Neuregulin-1/ErbB4 signaling regulates visual cortical plasticity. Neuron 92, 160-173 (2016).

 Kuhlman, S. J. et al. A disinhibitory microcircuit initiates critical-period plasticity in the visual cortex. *Nature* 501, 543–546 (2013).

- Sun, Y., Grieco, S. F., Holmes, T. C. & Xu, X. Local and long-range circuit connections to hilar mossy cells in the dentate gyrus. *eNeuro* https://doi. org/10.1523/ENEURO.0097-17.2017 (2017).
- Seidler, B. et al. A Cre-loxP-based mouse model for conditional somatic gene expression and knockdown in vivo by using avian retroviral vectors. Proc. Natl Acad. Sci. USA 105, 10137–10142 (2008).
- Madisen, L. et al. A robust and high-throughput Cre reporting and characterization system for the whole mouse brain. *Nat. Neurosci.* 13, 133–140 (2010).
- Tervo, D. G. et al. A designer AAV variant permits efficient retrograde access to projection neurons. Neuron 92, 372–382 (2016).
- Madisen, L. et al. A toolbox of Cre-dependent optogenetic transgenic mice for light-induced activation and silencing. *Nat. Neurosci.* 15, 793–802 (2012).
- Nguyen, A. Q., Dela Cruz, J. A., Sun, Y., Holmes, T. C. & Xu, X. Genetic cell targeting uncovers specific neuronal types and distinct subregions in the bed nucleus of the stria terminalis. *J Comp. Neurol.* https://doi.org/10.1002/ cne.23954 (2015).
- Xu, X., Roby, K. D. & Callaway, E. M. Mouse cortical inhibitory neuron type that coexpresses somatostatin and calretinin. *J. Comp. Neurol.* 499, 144–160 (2006).
- Xu, X., Roby, K. D. & Callaway, E. M. Immunochemical characterization of inhibitory mouse cortical neurons: three chemically distinct classes of inhibitory cells. *J. Comp. Neurol.* 518, 389–404 (2010).
- 62. Ikrar, T., Shi, Y., Velasquez, T., Goulding, M. & Xu, X. Cell-type specific regulation of cortical excitability through the allatostatin receptor system. *Front. Neural Circuits* **6**, 2 (2012).
- Ferguson, S. M. et al. Transient neuronal inhibition reveals opposing roles of indirect and direct pathways in sensitization. *Nat. Neurosci.* 14, 22–24 (2011).
- Krashes, M. J. et al. Rapid, reversible activation of AgRP neurons drives feeding behavior in mice. J. Clin. Invest. 121, 1424–1428 (2011).
- Richard, G. R. et al. Speed modulation of hippocampal theta frequency correlates with spatial memory performance. *Hippocampus* 23, 1269–1279 (2013).

- Buzsaki, G. Theta oscillations in the hippocampus. Neuron 33, 325–340 (2002).
- 67. Gomez, J. L. et al. Chemogenetics revealed: DREADD occupancy and activation via converted clozapine. *Science* **357**, 503–507 (2017).
- Mahler, S. V. & Aston-Jones, G. CNO evil? considerations for the use of DREADDs in behavioral neuroscience. *Neuropsychopharmacology* 43, 934–936 (2018).
- Lopez, A. J. et al. Promoter-specific effects of DREADD modulation on hippocampal synaptic plasticity and memory formation. *J. Neurosci.* 36, 3588–3599 (2016).
- Bui, A. D. et al. Dentate gyrus mossy cells control spontaneous convulsive seizures and spatial memory. Science 359, 787–790 (2018).
- 71. Vogel-Ciernia, A. & Wood, M. A. Examining object location and object recognition memory in mice. *Curr. Protoc. Neurosci.* **69**, 31–17 (2014).
- Pnevmatikakis, E. A. & Giovannucci, A. NoRMCorre: an online algorithm for piecewise rigid motion correction of calcium imaging data. *J. Neurosci. Methods* 291, 83–94 (2017).
- Zhou, P. et al. Efficient and accurate extraction of in vivo calcium signals from microendoscopic video data. *eLife* https://doi.org/10.7554/eLife.28728 (2018).
- Pnevmatikakis, E. A. et al. Simultaneous denoising, deconvolution, and demixing of calcium imaging data. Neuron 89, 285–299 (2016).
- Friedrich, J., Zhou, P. & Paninski, L. Fast online deconvolution of calcium imaging data. PLoS Comput. Biol. 13, e1005423 (2017).
- Mallory, C. S., Hardcastle, K., Bant, J. S. & Giocomo, L. M. Grid scale drives the scale and long-term stability of place maps. *Nat. Neurosci.* 21, 270–282 (2018).
- 77. Ismakov, R., Barak, O., Jeffery, K. & Derdikman, D. Grid cells encode local positional information. *Curr. Biol.* 27, 2337–2343 e2333 (2017).
- Srivastava, N., Hinton, G., Krizhevsky, A., Sutskever, I. & Salakhutdinov, R. Dropout: a simple way to prevent neural networks from overfitting. *J. Mach. Learn. Res.* 15, 1929–1958 (2014).
- Ioffe, S. & Szegedy, C. Batch normalization: accelerating deep network training by reducing internal covariate shift. *Proc. Int. Conf. Mach. Learn.* 37, 448–456 (2015).
- 80. Kingma, D. P. & Ba, J. Adam: a method for stochastic optimization. Preprint at *arXiv* https://arxiv.org/abs/1412.6980 (2017).



Corresponding author(s):	Xiangmin Xu, Douglas Nitz
Last updated by author(s):	Aug 4, 2019

Reporting Summary

Nature Research wishes to improve the reproducibility of the work that we publish. This form provides structure for consistency and transparency in reporting. For further information on Nature Research policies, see Authors & Referees and the Editorial Policy Checklist.

Sta	atis	tics					
For	all st	atistical analyse	es, confirm that the following items are present in the figure legend, table legend, main text, or Methods section.				
n/a	Cor	nfirmed					
	The exact sample size (n) for each experimental group/condition, given as a discrete number and unit of measurement						
	\boxtimes	A statement on whether measurements were taken from distinct samples or whether the same sample was measured repeatedly					
	\boxtimes	The statistical test(s) used AND whether they are one- or two-sided Only common tests should be described solely by name; describe more complex techniques in the Methods section.					
	\boxtimes	🔀 A description of all covariates tested					
	\boxtimes	🔘 A description of any assumptions or corrections, such as tests of normality and adjustment for multiple comparisons					
	A full description of the statistical parameters including central tendency (e.g. means) or other basic estimates (e.g. regression coefficient AND variation (e.g. standard deviation) or associated estimates of uncertainty (e.g. confidence intervals)						
	For null hypothesis testing, the test statistic (e.g. <i>F</i> , <i>t</i> , <i>r</i>) with confidence intervals, effect sizes, degrees of freedom and <i>P</i> value noted <i>Give P values as exact values whenever suitable.</i>						
\boxtimes	For Bayesian analysis, information on the choice of priors and Markov chain Monte Carlo settings						
\times	For hierarchical and complex designs, identification of the appropriate level for tests and full reporting of outcomes						
	Estimates of effect sizes (e.g. Cohen's d , Pearson's r), indicating how they were calculated						
	1		Our web collection on <u>statistics for biologists</u> contains articles on many of the points above.				
So	ftw	are and c	ode				
Poli	cy in	formation abou	nt <u>availability of computer code</u>				
Da	ata c	ollection	Brain section images were acquired using the MetaMorph or ZEN imaging acquisition software. Behavioral data were recorded by using ANY-maze (v. 4.99z) software. Ca++ Imaging data were acquired using custom-developed and validated software (http://miniscope.org/index.php/Data_Acquisition_Software)				
Data analysis		nalysis	Brain section images were analyzed using Metamorph, ZEN (black edition 2.3) and Adobe Photoshop CS4. Ca++ imaging data were preprocessed by using ImageJ 1.50i and analyzed using MATLAB based packages and scripts. MATLAB packages that were used for the manuscript include NoRMCorre for image motion correction, CNMF-E for Ca++ signal extraction, and OASIS for Ca++ signal				

For manuscripts utilizing custom algorithms or software that are central to the research but not yet described in published literature, software must be made available to editors/reviewers. We strongly encourage code deposition in a community repository (e.g. GitHub). See the Nature Research guidelines for submitting code & software for further information.

Data

Policy information about availability of data

All manuscripts must include a <u>data availability statement</u>. This statement should provide the following information, where applicable:

deconvolution. MATLAB 2016b or GraphPad Prism 5 was used to perform statistical analyses.

- Accession codes, unique identifiers, or web links for publicly available datasets
- A list of figures that have associated raw data
- A description of any restrictions on data availability

All data used for the current study are available from the corresponding author upon reasonable request.

	1	1			
<u>⊢ 14</u>	אוב	1_cna	CITIC	repoi	rtıng
1 17	こし	1-2PC		ICPUI	LILIE

Please select the o	ne below that is the best fit for your research. If you are not sure, read the appropriate sections before making your selection.			
∑ Life sciences ☐ Behavioural & social sciences ☐ Ecological, evolutionary & environmental sciences				
For a reference copy of	For a reference copy of the document with all sections, see nature.com/documents/nr-reporting-summary-flat.pdf			
Life scier	nces study design			
All studies must dis	sclose on these points even when the disclosure is negative.			
Sample size	The cell samples and animal numbers were based on estimation from previous studies, including our own published studies.			
Data exclusions	The "a priori" criteria are defined before executing experiments for rational inclusion/exclusion of data, as established in our published studies. Specifically, for anatomical tracing and behavioral experiments involving virus-mediated gene expressions, individual cases that were off the target region or did not have sufficient expression were excluded. Also, exclusion was applied to one mouse that developed a monocular cataract in one of our experiments.			
Replication	Experiments were repeated, and the results are reproducible. Viral tracing, imaging and behavioral studies were conducted using different cohorts of animals. The outcomes are consistent, and results are robust.			
Randomization	Mice were randomly assigned to experimental vs. control groups with matched age and sex, whenever possible.			
Blinding	Experimenters were not blinded during data acquisition, but imaging data and behavioral data analyses were performed blind to treatment.			

Reporting for specific materials, systems and methods

We require information from authors about some types of materials, experimental systems and methods used in many studies. Here, indicate whether each material, system or method listed is relevant to your study. If you are not sure if a list item applies to your research, read the appropriate section before selecting a response.

Materials & experimental systems			Methods		
n/a	a Involved in the study		Involved in the study		
	X Antibodies	\boxtimes	ChIP-seq		
\boxtimes	Eukaryotic cell lines	\boxtimes	Flow cytometry		
\boxtimes	Palaeontology	\boxtimes	MRI-based neuroimaging		
	Animals and other organisms		•		
\boxtimes	Human research participants				
\boxtimes	Clinical data				

Antibodies

Antibodies used

All antibodies used in the current study have been described in detail in the Methods. The primary antibodies include: chicken anti-GFP polyclonal antibody (Aves Labs, 1:500 dilution, Cat# GFP-1010,)

mouse anti-NeuN monoclonal antibody, clone A60 (Millipore, 1:100 dilution, Cat# MAB377)

rabbit anti-GABA polyclonal antibody (Sigma-Aldrich, 1:1000 dilution, Cat# A2052)

rabbit anti-dsRed polyclonal antibody (Clontech, 1:250 dilution, Cat# 632496)

rabbit anti-CaMKII polyclonal antibody M-176 (Santa Cruz Biotechnology, 1:500 dilution, Cat# sc-9035)

rat anti-SST monoclonal antibody, clone YC7 (Millipore, 1:200 dilution, Cat# MAB354)

All the secondary antibodies used in this study were purchased from Jackson ImmunoResearch. We used them with a dilution of 1.200

Alexa Fluor® 488 AffiniPure Donkey Anti-Chicken IgY (IgG) (H+L) (Cat# 703-545-155)

Alexa Fluor® 488 AffiniPure Donkey Anti-Mouse IgG (H+L) (Cat# 715-545-150)

Alexa Fluor® 488 AffiniPure Donkey Anti-Rabbit IgG (H+L) (Cat# 711-545-152)

Alexa Fluor® 647 AffiniPure Donkey Anti-Rabbit IgG (H+L) (Cat# 711-605-152)

Cy™3 AffiniPure Donkey Anti-Rabbit IgG (H+L) (Cat# 711-165-152)

Alexa Fluor® 488 AffiniPure Donkey Anti-Rat IgG (H+L) (Cat# 712-545-150)

Validation

Our primary antibodies used in our immunostaining experiments are commercially available from major companies which provide extensive validation data (below). Please also see our previous publications (Xu et al., 2006 and 2010; Nguyen et al., 2015; Sun et al., 2016; 2018) for detailed information regarding the antibody characterization and specificity. We often confirm antibody specificity using immunoabsorption tests and validated using mutant mice when available.

For chicken anti-GFP polyclonal antibody, Aves Labs provides validation information as follows

"Antibodies were analyzed by western blot analysis (1:5000 dilution) and immunohistochemistry (1:500 dilution) using transgenic mice expressing the GFP gene product. Western blots were performed using BlokHen® (Aves Labs) as the blocking reagent, and HRP-labeled goat anti-chicken antibodies (Aves Labs, Cat. #H-1004) as the detection reagent. Immunohistochemistry used tetramethyl rhodamine-labeled anti-chicken IgY"

For mouse anti-NeuN monoclonal antibody, Millipore provides validation information as follows "MAB377 reacts with most neuronal cell types throughout the nervous system of mice including cerebellum, cerebral cortex, hippocampus, thalamus, spinal cord and neurons in the peripheral nervous system including dorsal root ganglia, sympathetic chain ganglia and enteric ganglia. The immunohistochemical staining is primarily in the nucleus of the neurons with lighter staining in the cytoplasm. The few cell types not reactive with MAB377 include Purkinje, mitral and photoreceptor cells."

For rabbit anti-dsRed polyclonal antibody, Clontech provides validation information as follows "The quality and performance of this lot of Living Colors DsRed Polyclonal Antibody was tested by Western blot analysis. Lysate (10 μ l; equivalent to 35,000 cells) from untransfected HEK 293 cells and lysates (10 μ l; equivalent to 35,000 cells) from HEK 293 cells stably expressing DsRed-Express or AcGFP1 were resolved on a 12% SDS polyacrylamide gel and then transferred to a nitrocellulose membrane. The membrane was probed with the Living Colors DsRed Polyclonal Antibody (diluted 1:1,000), followed by secondary goat anti-rabbit antibody conjugated to horseradish peroxidase. The HRP signal was detected by chemiluminescence. A specific band of approximately 30–38 kDa was observed in the lane loaded with lysate from cells expressing DsRed-Express. No band in this molecular weight range was detected for the lysates of the untransfected HEK 293 cells or the cells expressing AcGFP1."

For rat anti-SST monoclonal antibody, Millipore provides validation information as follows "Shows no cross-reactivity to enkephalins, other endorphins, substance P or CGRP. Partially cross-reacts with somatostatin fragments"

Animals and other organisms

Policy information about studies involving animals; ARRIVE guidelines recommended for reporting animal research

Laboratory animals All mi

All mice used were the C57BL/6 background strains of either sex at 8-12 weeks old. Ai9 mice were used for CAV2-Cre verification. Ai32 mice were used for in vivo optogenetic experiments. Camk2a-Cre were used for in vitro validation of genetic manipulation methods. Other experiments were performed using C57BL/6J mice with virus infections. Please see detailed descriptions in Supplementary Table 4.

Wild animals

No wild animals were used in this study

Field-collected samples

No field-collected samples in this study

Ethics oversight

All experiments were conducted according to the National Institutes of Health guidelines for animal care and use and were approved by the Institutional Animal Care and Use Committee and the Institutional Biosafety Committee of the University of California, Irvine.

Note that full information on the approval of the study protocol must also be provided in the manuscript.